[American Journal of Science, Vol. 315, May, 2015, P. 412–459, DOI 10.2475/05.2015.02]

THE GEODYNAMICS OF FAULTS AND PETROLEUM MIGRATION IN THE LOS ANGELES BASIN, CALIFORNIA

BYEONGJU JUNG*,†, GRANT GARVEN**, and JAMES R. BOLES***

ABSTRACT. A two-dimensional multiphase fluid flow model, coupled with heat flow, using a hybrid finite element and finite volume method is developed and applied to fundamental issues of long-distance petroleum migration and accumulation in the Los Angeles basin, which is intensely faulted and deformed by transpressional tectonic stresses, yet host to the world's richest oil accumulation.

These simulations show that a combination of continuous hydrocarbon generation and primary migration from upper Miocene (~10 – 5 Ma) source rocks in the central Los Angeles basin synclinal region, coupled with subsiding basin fluid dynamics, favored the massive accumulation and alignment of hydrocarbon pools along the Newport-Inglewood fault zone (NIFZ). According to our multiphase flow calculations, the maximum formation water velocity within fault zones likely ranged between 0.5 to 1.0 m/yr during the middle Miocene to Pliocene epochs (13–2.6 Ma). The estimated time for long-distance (~25 km) petroleum migration from source beds in the central basin to oil fields along the NIFZ is approximately 90,000 to 220,000 years, depending on the effective permeability assigned to the faults (5 ~ 50 md) and adjacent inter-bedded sandstone and siltstone "petroleum aquifers." With an average long-distance flow rate of 0.2 m/yr and fault permeability of 20 md (2.0×10^{-13} m^2), the total petroleum volume of the Inglewood oil field (450 million barrels $\approx 1.6 \times 10^5$ m^3) would have accumulated over a period of 180,000 years or less. The results also suggest that besides the thermal and structural history of the basin, the fault permeability, capillary pressure, and the configuration of aquifer and aquitard layers played an important role in controlling petroleum migration rates, patterns of flow and saturation, and the overall fluid mechanics of petroleum accumulation.

Keywords: petroleum migration, fluid flow in faults, multiphase flow.

INTRODUCTION

The structural geology of large-scale faults affects deep fluid migration and the distribution of hydrocarbon reservoirs. Faults develop interlinked channels for hydrocarbon fluids if connected with juxtaposed heterogeneous strata. Evidence for fluid discharge is abundant in basins. Examples include oil and gas seeps, geothermal springs, hydrothermal deposits and mineralized veins in fault zones (Sorkhabi and Tsuji, 2005).

Long-distance petroleum migration in sedimentary basins in North America is also commonly associated with large-scale fault zones and interconnected aquifers. Many oil fields are located tens of kilometers away from their source rocks (Tissot and Welte, 1984; Garven, 1989; Ungerer and others, 1990; Bethke and others, 1991; Carruthers and Ringrose, 1998; Carruther, 2003). Bethke and others (1991) reported clear association of long-range petroleum migration in the Illinois basin, and other

* Geologic Environment Division, Korea Institute of Geoscience and Mineral Resources (KIGAM), 124 Gwahak-ro, Yuseong-gu, Daejeon 305-350, South Korea.

** Department of Earth and Ocean Sciences, Tufts University, 105 Lane Hall, Medford, Massachusetts 02155; Tel: +1 617 627 3795, Email: grant.garven@tufts.edu.

*** Department of Earth Science, University of California, Santa Barbara, California 93106; Tel: +1 805 893 3471, Email: boles@geol.ucsb.edu.

† Corresponding author: Email: bjung@kigam.re.kr; Tel: +82 42 868 3635.

sedimentary basins in the mid-continent region of North America. In the Williston basin, Dow (1974) argued that petroleum migrated more than 150 km from its source beds. Similar distances of petroleum migrations are also reported for the Denver basin (Clayton and Swetland, 1980) and the Alberta basin, Canada (Moshier and Waples, 1985; Garven, 1989; Creaney and Allan, 1990; Demaison and Huizinga, 1991; Creaney and others, 1994; Larter and others, 1996).

Geochemical evidence suggests that petroleum takes advantage of permeable faults and aquifer connections in sedimentary basins. Diagenetic processes such as calcite mineralization in faults is sometimes a good indicator of hydrocarbon migration. For example, the carbon isotopic composition in calcite veins found in the Santa Barbara basin confirms that most of the carbon in the calcite mineralization is derived from thermogenic methane, focused by fluid flow into the fault zone (Boles and Ramseyer, 1987; Boles and others, 2004). Diagenetic carbonates are also reported in the Los Angeles basin, and can be a useful fabric to characterize the geohydrology of the basin and the role of large-scale faults. Other geochemistry data and biomarker analyses from both oil and source rock samples also support the notion of long-distance petroleum migration in the Los Angeles basin area (Kaplan and others, 2000).

Despite extensive study, the dynamics of petroleum migration remains to be a mostly qualitative science. A clearer understanding of fluid migration in the deep subsurface is necessary to explore new energy sources such as methane hydrate and shale gas, and also to predict the long-term fate of injected carbon dioxide into the subsurface to contain greenhouse gases.

This study is not the first attempt to model petroleum migration quantitatively. It has been studied for many decades (Munn, 1909; Rich, 1921; Hubbert, 1953; Hodgson, 1980; Tóth, 1980, 1987, 1988; Garven, 1989; England and Fleet, 1991; Harrison and Summa, 1991; Person and Garven, 1992; Hayba and Bethke, 1995; Sanford, 1995; Garden and others, 2001; Ingebritsen and others, 2006; Karlsen and Skeie, 2006; Tóth, 2009; Manzocchi and others, 2010; Person and others, 2010). Hubbert (1953) first quantified the hydrodynamics and physics governing immiscible secondary petroleum migration, showing that the impelling force contains both a hydromechanic potential difference and a buoyancy effect. Tóth (1980) expanded the concept of "hydraulic theory of petroleum migration" and argued that hydrocarbon movements are strongly affected by regional groundwater flow. Tóth's early studies largely contributed the conceptualization of petroleum migration and trapping settings in a more hydrogeologic perspective. Person and Garven (1989) and Hayba and Bethke (1995) modeled the migration process at a large scale, covering the entire sedimentary basin and obtained reasonable estimations on accumulated petroleum mass and migration speed. Karslen and Skeie (2006), and Manzocchi and others (2010) added more structural complexities in their simulations and showed that large-scale faults can affect both the migration and entrapment aspects of petroleum systems.

Unlike the above studies, we attempt to quantitatively characterize petroleum generation and migration in the Los Angeles basin using combined numerical approaches simulating sedimentary compaction and basin-scale multiphase flow coupled with heat transport. We also used a newly constructed hydrogeological profile and consider large-scale fault zones in the simulation, for understanding the role of the faults on the migration process. Our hypothesis is oil reservoirs along the major faults in the Los Angeles basin are mostly formed as the result of long-distance migration. During this process, both clastic aquifer and large-scale faults act as effective conduits from the source rock to the reservoir trap.

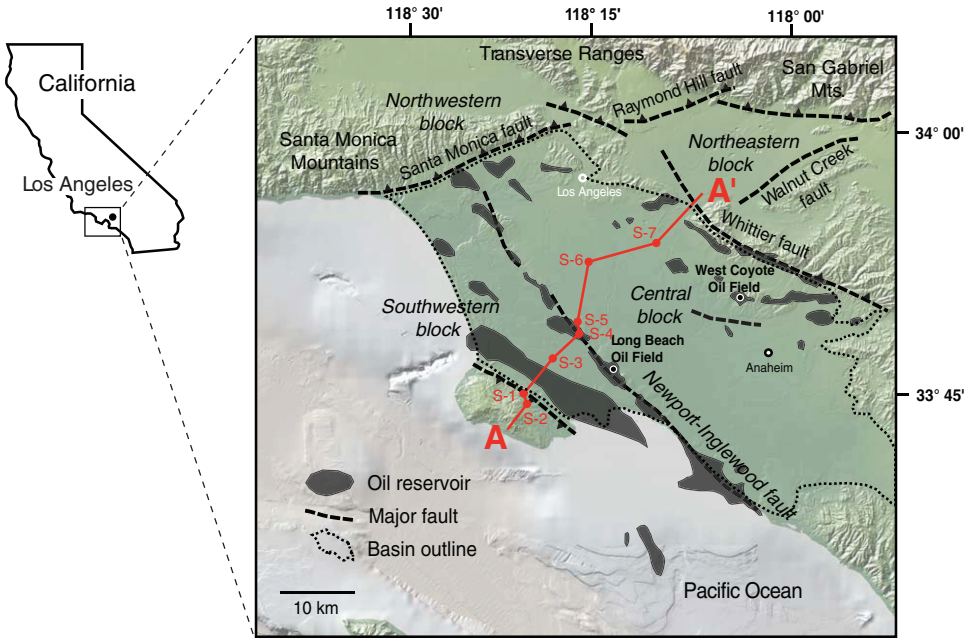

Fig. 1. The location of the Los Angeles basin showing hydrocarbon reservoirs associated with large-scale fault zones (modified from Biddle, 1991). The background elevation map was generated by Global Multi-Resolution Topography (GMRT) Synthesis (Ryan and others, 2009).

The Newport-Inglewood fault zone (NIFZ) and Los Angeles basin were chosen for the research because the correlation between oil reservoirs and fault structures is particularly prominent. Major hydrocarbon reservoirs (for example Inglewood, Dominguez, Long Beach, Sunset Beach, Seal Beach, Huntington Beach) are spatially aligned along the trend of NIFZ (fig. 1). Hydrogeologic conditions at depth along the fault zone are still under investigation and being explored by deep drilling exploration, but the geographic correlation between the fault and reservoirs support the hypothesis that the basin's petroleum system is strongly structurally controlled.

Here in this study, we first simulate sediment compaction in the basin to predict both geopressures and geothermal conditions, and likely source rock maturation during subsidence and burial. Then we develop a multiphase flow model to estimate petroleum flow patterns and the time for regional migration and reservoir formation. The developed multiphase flow model is based on a hybrid finite element-finite volume approach (Huber and Helmig, 2000; Reichenberger and others, 2006; Geiger and others, 2006a, 2006b) based on the implicit pressure-explicit saturation (IMPES) numerical scheme (Aziz and Settari, 1979; Chen and others, 2006) and includes capillarity and other nonlinear effects between fluid phases.

GEOLOGIC SETTING

The Los Angeles basin is a pull-apart sedimentary basin formed between northwest-trending right-lateral strike-slip faults having a similar orientation to the San Andreas Fault and east-west left-lateral faults bounded by the Transverse Ranges. It is within the active transform boundary zone, and deformation is ongoing due to the relative motion of the North American and Pacific plates (Wright, 1991; Griffith and Cooke,

2005; Fisher and others, 2009). The northern part of the Los Angeles basin is bounded by the Peninsular Ranges, which are composed of metamorphosed sedimentary and volcanic rocks of Jurassic age that were later intruded by Cretaceous plutonic rocks. The southern part of the basin is part of the onshore California continental borderland, which includes many northwest-trending ridges and basins formed in the Miocene (Schoellhammer and others, 1981; Wright, 1991; Crouch and Suppe, 1993). The basin extends from the San Joaquin Hills and Santa Ana Mountains in the south and merges with the Ventura basin in the north. The thickness of Neogene sedimentary fill in the central syncline of the basin is about 9 km and thins near the edges (Yerkes and others, 1965). Major regional-scale strike-slip faults such as the Newport-Inglewood, Whittier, and Palos Verdes faults dominate the structure of the western basin margin. The Los Angeles basin has been extensively studied for decades because of the prolific hydrocarbon production in this region (Biddle, 1991; Norris and Webb, 1990; Bilodeau and others, 2007).

The Los Angeles basin can be divided in four structural blocks, and the boundaries among the blocks are large-scale fault zones resulting from the tectonic movement of Pacific and North American plates (fig. 1). The northwestern block includes parts of the east-trending Santa Monica Mountains and the San Fernando Valley. The Santa Monica-Raymond Hill-Cucamonga thrust fault separates the block from the other three blocks. The southwestern block and the central block are separated by the Newport-Inglewood fault zone, and the NIFZ is believed to merge with a deep concealed thrust fault in the Catalina Schist (Davis and others, 1989; Shaw and Suppe, 1996; Griffith and Cooke, 2005) (fig. 2). The northeastern block is bounded by the Whittier fault and the Santa Monica-Raymond Hill-Cucamonga fault.

The Los Angeles basin opened by the rifting and rotating motion of the surrounding plates (Luyendyk and Hornafius, 1987; Geiser and Seeber, 2008; Fisher and others, 2009; Cooke and Dair, 2011). Regional tectonic events and their deformational history since the Eocene are illustrated in figure 3. The initial opening of the basin started in the early Miocene (20–18 Ma), and massive continental and marine sediments were rapidly deposited during extensional deformation (Crouch and Suppe, 1993; Ingersoll and Rumelhart, 1999; Bilodeau and others, 2007). The next extensional deformation began in the late Miocene-Pliocene (6–3 Ma). This tectonic movement opened the Gulf of California and transformed southern California into a region of right-slip faults following the San Andreas transform fault trend. After these two episodes of extension, north-south tectonic compression began in the late Pliocene-Pleistocene. It produced major uplift and crustal shortening along an east-west trend. This Plio-Pleistocene transpressional deformation, locally known as Pasadena deformation (Yerkes and others, 1965; Wright, 1991), reactivated many Miocene detachment faults as low-angle thrusts (Crouch and Suppe, 1993), and created most of the modern topography in the area including the San Gabriel and Santa Monica Mountains and the Puente, Palos Verdes, and Dominquez Hills.

The stratigraphic nomenclature of the Los Angeles basin varies by location and researcher (Yerkes, 1972; Schoellhammer and others, 1981). We will follow nomenclature guided by the general lithology rather than using formation names derived from detail biostratigraphic criteria. The Los Angeles basin is underlain by Cretaceous crystalline basement rocks (Catalina Schist and granite plutons). Extension on high angle faults created the basin that was later filled with thick accumulation (over 10 km) of Miocene to Pleistocene sediments (fig. 4). The sediment was deposited under mostly marine environments.

Miocene sediments of the Los Angeles basin can be divided generally into lower and upper Miocene sequences (Campbell and Yerkes, 1976; Fritsche, 1998). The lower Miocene strata are mostly the Topanga Formation, which is deposited on granitic

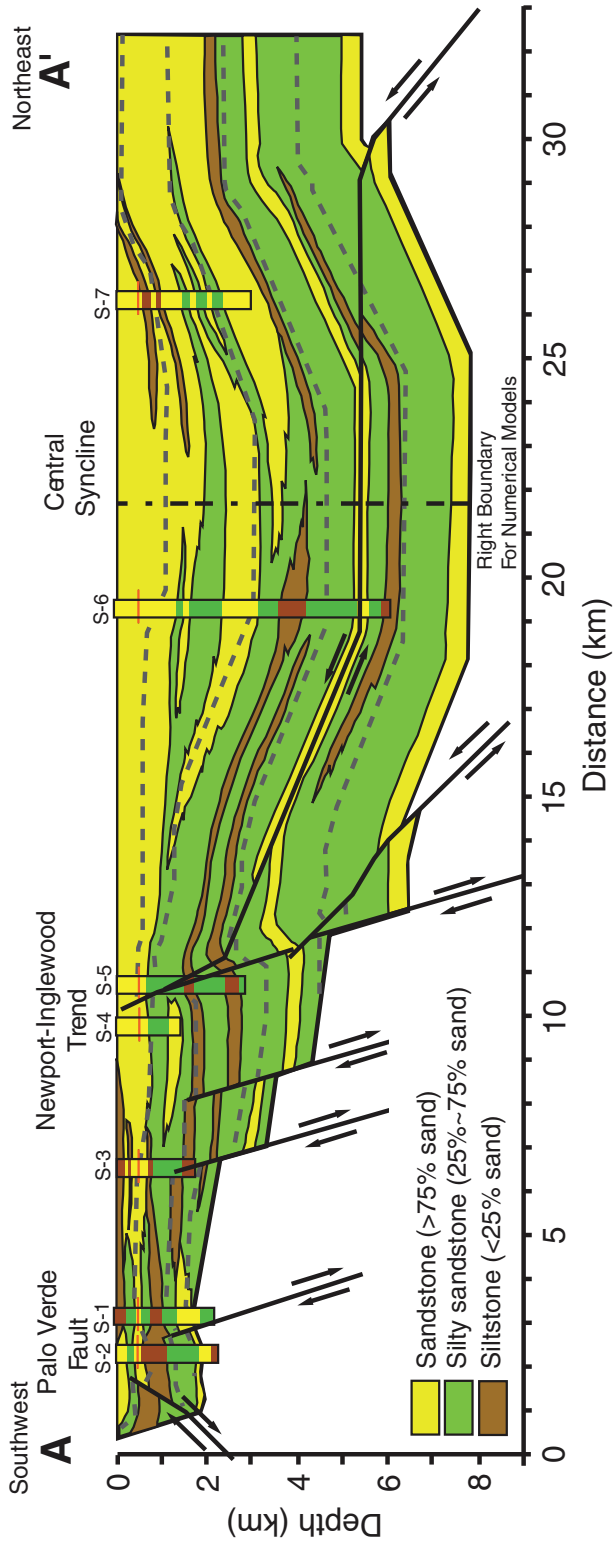

Fig. 2. Hydrogeologic cross section through the LA basin along A-A' (see fig. 1). The structural base map was adopted from Shaw and Suppe (1996).

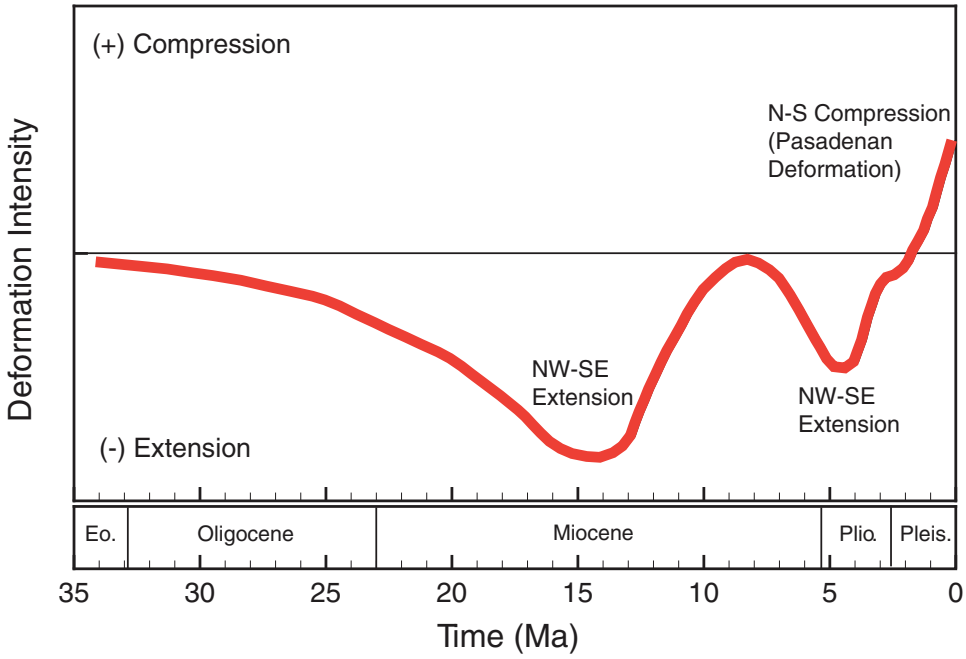

Fig. 3. Tectonic history of the LA basin (modified from Wright, 1991). Extensional deformation began in the early Miocene. North-south compression started in the late Pliocene and continues to the present.

basement in the central block. It consists of a few kilometers of thick layers dominated by sandstone and locally includes shallow marine sediments. The thickness of the Topanga Formation varies by location, but on average it reaches about 2 km in the San Joaquin Hills of the central block and decreases to about 0.6 km at the boundary of the southwestern block. The Topanga Formation unconformably overlies the basement, with fine-grained clastic rocks at its base (Fritsche, 1998; McCulloh and others, 2000).

The upper Miocene sequences include the stratigraphically equivalent Modelo, Monterey, and Puente Formations. All of these stratigraphic units are deposited in an upper to middle bathyal environment and consist of hemipelagic and clastic sediments (Blake, 1991). The Monterey Formation that occurs in the central block consists of siliceous siltstone and shale grading up to micaceous siltstone and sandstone. In the southwestern block, the Monterey Formation is lithologically more diverse. The lower members that were deposited in the middle to late Miocene are mainly silty and sandy shale with intercalated limestone and dolomite layers. The upper members are laminated diatomite and phosphatic shale with minor amounts of calcite and dolomite and very high content of organic compounds (TOC 2-18%) (Redin, 1991). The dominant organic materials are sapropelic sediments with high capacity for oil generation and production (Welte and Yükler, 1980). Other time-equivalent strata in the Los Angeles basin share similar lithologic characteristics with the Monterey Formation. The thicknesses of these units are about 2.3 km at the depocenter, thinning to 0.7 km towards the southwest. Due to the high total organic carbon content, these upper Miocene to lower Pliocene sedimentary rocks are considered as the primary source rocks for hydrocarbons in the Los Angeles basin.

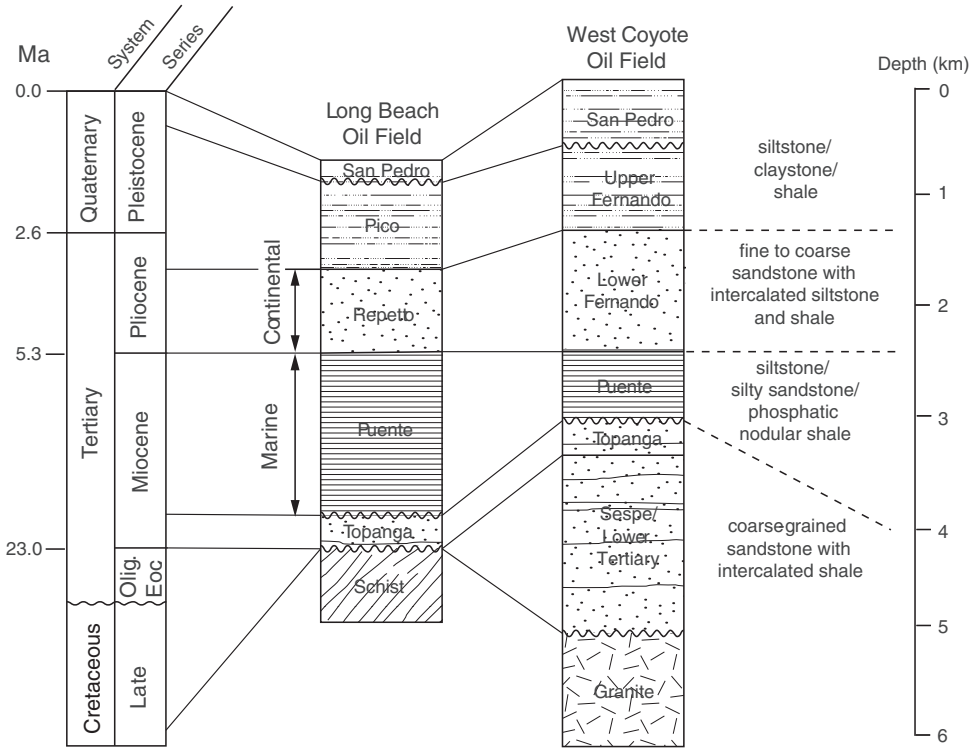

Fig. 4. Geologic age, hydrostratigraphic and lithologic description of sedimentary formations along the section A-A′ (modified from Redin, 1991).

The Pliocene and Pleistocene sediments are difficult to subdivide lithologically, because there is little variation through the stratigraphic section. Instead, biostratigraphic subdivision by benthic faunal assemblages is used to determine the boundary between the Repetto and Pico Formations. The Repetto Formation is the most laterally extensive Pliocene unit in the Los Angeles basin. The formation ranges in thickness about from 0.3 km to over 5.0 km and consists of massive siliciclastic sediments including marine silt, sand, and gravel (Blake, 1991; Bilodeau and others, 2007). The maximum rate of subsidence was attained during deposition of the lower Repetto units that are a part of a submarine fan complex (Redin, 1991). In the central plain, deposition seems to have been uninterrupted during the late Pliocene. In marginal areas, however, tectonic activity along the boundary faults (for example the Newport-Inglewood and Whittier faults) created an unconformity in the upper unit of the Repetto Formation (Yerkes, 1972). The Pico Formation includes the upper Pliocene and Pleistocene sediments, and is deposited in upper bathyal to neritic environments; the lithology of the Pico Formation is similar to Repetto and consists mostly of inter-layered siltstone and shale.

A stratigraphic cross section that profiles the basin from the west to east (along S1 to S7 in fig. 1) is illustrated in figure 2. This stratigraphic profile is based on geophysical surveys and structural and stratigraphic interpretations by Shaw and Suppe (1996), and further refined by geophysical borehole logs obtained by the authors. Well specifications and logging methods are organized in table 1. The numerical grids for the models are designed based on this stratigraphic-structural cross section.

TABLE 1

List of boreholes on the cross section in figure 2

Well No. (Fig. 3.2)	Well Name	API Number	Section-Township-Range	Depth Range (ft)	Log Suite‡
S-1	Chandler-MacBurney No.1	3706238	35-4s-14w	750-1500	SP-RES
S-2	Sidebotham No. 1	3706116	35-4s-14w	100-7243	SP-RES
S-3	Marigold No. 2	3705626	7-4s-13w	314-5540	SP-RES
S-4	Reyes-deFrancis No. 1	3706912	34-3s-13w	850-4370	SP-RES-IND-COND
S-5	Hellman No. 67	3706174	27-3s-13w	951-9030	SP-RES
S-6	Central C. H. No. 1	3721520	4-3s-13w	100-19800	SP-RES-IND-COND
S-7	Weiser No. 1	3706004	20-2s-12w	100-3920	SP-RES-IND-COND

‡ SP: Spontaneous potential log; RES: Resistivity log; IND: Induction log; COND: Conductivity log.

The Newport-Inglewood fault zone is one of the best-known structural features of the Los Angeles basin. It trends roughly N45 °W and extends about 64 km southeast from Culver City to Newport Beach. Many small folds and faults occur along a strike-slip fault plane. Estimated horizontal displacement along the fault plane is approximately 1.5 km (Norris and Webb, 1990). The fault is linked to a deep underlying master thrust fault, which was probably formed during the early Pliocene deformation (Davis and others, 1989).

Deformation remains active at present, and earthquakes are frequently recorded in the Long Beach area. Shaw and Suppe (1996) were able to structurally restore the basin to its early Pliocene configuration by calculating the slip rate of the master detachment (Central Basin Décollement) using regional seismic images. They concluded that the current deformation signature of the basin can be explained by kinking and thrusting mechanisms associated with compressional and transpressional deformation.

The Los Angeles basin is one of the most productive basins in terms of hydrocarbons recovered per unit volume of sediments. The estimated ultimate recovery (EUR) is about 4 million barrels (MMbbl) per cubic mile of sediments. Total recovery from over 60 oil and gas fields in the basin is estimated to be more than 10 billion barrels (10 Gbbl), and the Wilmington field, the largest reservoir, contains over 3 Gbbl alone (Biddle, 1991).

The petroleum productivity of the Los Angeles basin has resulted from the organic-rich source rocks, reduced condition, and thermal history of the basin. Differential tectonic subsidence accompanied by sea level rise created many isolated sub-basins that provided ideal environments for accumulating biogenic and organic-rich sediments (Biddle, 1991). Relatively small basins had restricted circulation causing reducing conditions for preserving organic materials. The average TOC content is as high as 10 percent in many productive Miocene formations such as Modelo, Puente, and Monterey (Jeffrey and others, 1991; Kaplan and others, 2000).

SOURCE ROCK MATURITY AND EVIDENCE OF PETROLEUM MIGRATION

Geochemical evidence from the analysis of source rocks, oil and gas, and biomakers can provide conceptual models and constraints for petroleum migration in the Los Angeles basin. Both TMAX temperature and vitrinite reflection index are good indicators of thermal maturity of source rock (Tissot and others, 1987). Source rocks are generally considered immature if TMAX values are under 435 °C but in some cases calibration for compensating mineral matrix effects is needed. Similarly, source rocks are considered immature if vitrinite reflectance (R_o) is greater than 0.5 (Hunt, 1979).

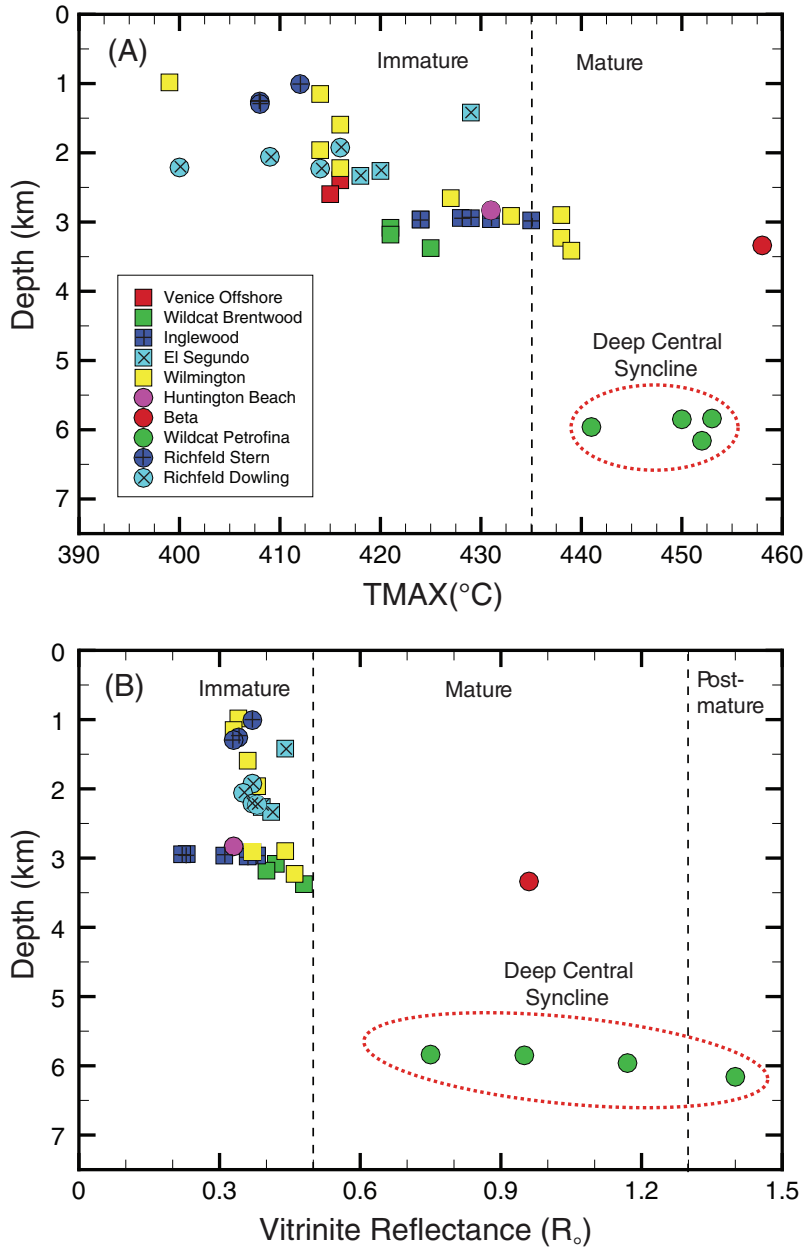

Fig. 5. Thermal maturity data obtained from the LA basin source rocks: (A) TMAX (B) vitrinite reflectance (modified from Kaplan and others, 2000).

Figures 5A and 5B show TMAX and R_o values of source rock samples obtained from various oil reservoirs in the Los Angeles basin (adopted from Kaplan and others, 2000). The majority of source rocks located near the edges of the basin are either immature or marginally mature, although they contain a significant amount of organic matter having oil-producing potential. Only samples taken from the deep central

syncline are considered fully mature. The mostly mature TMAX and R_o values of petroleum samples taken from the same locations (Kaplan and others, 2000) suggest that petroleum, which matured in the deep central basin, migrated toward the edge of the basin where source rocks are not yet matured. The fact that the samples obtained from the lower parts of Huntington Beach and Inglewood oil fields are marginally mature can be explained by the relatively high geothermal gradient along the Newport-Inglewood fault zone and may also be indicative of vertical leakage of basin fluids from the deep area (Williams and others, 2001).

FAULT-ENHANCED PETROLEUM MIGRATION

The relationship between faults and petroleum migration/entrapment has been noted elsewhere (Sorkhabi and Tsuji, 2005). It is also known that most of the oil-producing zones in the Rhine graben in Germany are located adjacent to normal faults, and this strongly suggests the impact of fracture-controlled basinal flow on petroleum migration (Person and Garven, 1992). Another example demonstrating the influence of large-scale faults on secondary oil migration is the Halten Terrace area in Norway (Karlsen and Skeie, 2006). This region, similar to the Los Angeles basin, has large-scale paleo-active normal fault zones currently associated with productive hydrocarbon reservoirs. In the North Sea, over 40 percent of successful petroleum exploration wells have been reported in seismically discernible fault zones. However, their success rate is only 10 percent in areas distal from the fault zone (Leonard, 1984).

The general theory of primary and secondary petroleum migration is well described by Hubbert (1953), who showed that the driving force for petroleum movement depends on the fluid potential (mechanical energy per unit mass). Buoyant forces make petroleum move upward with increased speed, and their magnitude is proportional to the density difference between groundwater and oil at a given P-T condition. As the petroleum density is a function of pressure, temperature, and composition, the buoyant forces also vary depending on those conditions. Capillary forces are the dominant control on large-scale petroleum migration and especially will be a dominant restraining force when the petroleum encounters rocks with small size pores such as shale or mudstone (Hubbert, 1953; Bear, 1972; England and others, 1987; Carruthers and Ringrose, 1998; Carruthers, 2003; Cavanagh, 2013).

In petroleum geology, a fault can be characterized as either a fluid conduit or a barrier in the subsurface, and for both cases it plays a very important role in the migration of petroleum. If the fault is a fluid barrier, it can seal the lateral or vertical movement of petroleum and create compartmentalized reservoirs that offer enough economic advantages to be explored and developed. If the fault acts as a fluid conduit, petroleum can migrate long distances and form giant reservoirs. The Los Angeles basin is a very good example of temporal changes in both roles of a fault. Petroleum traps in the Los Angeles basin were formed during the early phases of extension associated with middle Miocene trans-tensional strike-slip and the later phase of tectonic compression after the Pliocene (Wright, 1991). During the extensional deformation (Miocene-Pliocene), a set of basin-scale normal faults could have served as conduits linking to the deep central basin where geochemists inferred the greatest amount of petroleum had been initially generated. Once these structural channels had been established, a large amount of petroleum could have migrated and saturated sand/sandstone formations. In later stages of the basin history, those faults were reactivated by transpressional plate deformation and accelerated the regional hydrocarbon migration. At a reservoir scale, however, the entrapment of petroleum was enhanced by anticlinal structures and reverse faults associated with tectonic shortening. In addition, geochemical processes such as hydrothermal-diagenetic reactions and cementing also can expedite sealing the faults in oil reservoirs as the basin subsides, buried, and structurally deforms.

According to lab experiments and field observations, faults behave as conduits when they are actively deforming (Aydin, 2000; Sorkhabi and Tsuji, 2005). However, the high permeability of an active fault does not last for a long period of time because of mineralization (Sibson, 1977, 1994). Mineral precipitation seals the fracture aperture and decreases the permeability rapidly. Hydrocarbon-related calcite veins are observed in many locations in southern California, and these structures provide solid evidence for fluid flow along the fractures (Boles and others, 2004; Perez and Boles, 2007; Eichhubl and others, 2009). Cemented faults are susceptible to breakage, due to subsequent fracturing or pulses of compactional- or seismically-driven fluid flow, which may cause a repetition of the crack opening and sealing cycle.

To further understand the hydrodynamic role of faults, we propose two different numerical calculations. First, a basin compaction model is constructed to estimate the pressure/temperature fields created by the sediment loading and tectonic subsidence. From this model we predicted spatial and temporal changes of overpressures, which is one of the driving forces for the secondary petroleum migration. This model is coupled with basin heat flow, and the estimated temperature field is used to calculate organic maturation levels and to identify probable hydrocarbon source regions in the basin. Second, a basin-scale petroleum migration model shows how systematic linkage between faults and aquifers affects the physics of petroleum migration in a faulted basin. We apply a combined finite element and finite volume hybrid method with an implicit pressure-explicit saturation (IMPES) iterative scheme to deal with nonlinearity of phase saturation and capillary pressure.

GEOHYDROLOGIC EVOLUTION OF THE LOS ANGELES BASIN

Basin Compaction Model (Model I)

The theory of fluid flow in a compacting basin undergoing burial is well documented (Domenico and Palciauskas, 1979; Bethke, 1985; Person and Garven, 1992; Neuzil, 2003). Overpressures in a sedimentary basin are generated primarily by mechanical processes of sediment compaction, but other factors such as clay dehydration, thermal fluid expansion, and geochemical maturation processes are also important (Wilson and others, 1999). Sediment compaction induces porosity decrease in the consolidating medium, and pore pressure increases to compensate for the effective stress decrease (that is, mechanical compaction). As the sediments become more deeply buried, elevated temperature also contributes to generate overpressure by expansion of the fluid volume in a fixed pore structure (Domenico and Palciauskas, 1979; Swarbrick and others, 2002).

The numerical code RIFT2D (Person and Garven, 1994) is used here to investigate geohydrologic changes in the LA basin during its evolution. It can simulate compaction-driven groundwater flow as well as topography- and buoyancy-driven flows for any 2-D profile of a sedimentary basin. The equation governing fluid flow (conservation of mass) considers effective stress, thermal expansion of fluid, and kerogen-transformation terms (Person and Garven, 1994),

$$\frac{\partial(\rho\phi)}{\partial t} = -\nabla \cdot (\rho \mathbf{q}) + \Gamma \qquad (1)$$

where the left side represents the rate of fluid mass accumulation per unit bulk volume, and the first and second terms on the right side represent the net outflow of fluid mass associated with external driving forces and internal fluid sources(−)/sinks(+) per unit volume. For two-dimensional flow, Darcy fluxes in horizontal and vertical directions (q_x, q_z) can also be expressed in terms of pressure

$$q_x = -\frac{k_x}{\mu_f}(\nabla p_f), \quad q_z = -\frac{k_z}{\mu_f}(\nabla p_f + \rho_f g \nabla z) \tag{2}$$

where k_x and k_z are intrinsic permeabilities in x and z directions, p_f is pore fluid pressure and ρ_f and μ_f are fluid density and dynamic viscosity, respectively. The parameter g is the gravitational acceleration. The last term in equation 2 represents additional sources/sinks of fluid associated with mechanical compaction, fluid expansion, and volumetric changes of kerogen converting into liquid petroleum, respectively, which can be expressed as (Person and Garven, 1994):

$$\Gamma = -\frac{1}{E\rho_s g}\frac{\partial \sigma_v}{\partial t} - \phi\Lambda\frac{\partial T}{\partial t} + \frac{(\rho_k - \rho_{oil})}{\rho_f}\frac{\partial R_t}{\partial t} \tag{3}$$

where E is the one-dimensional elastic deformation modulus of the medium, ϕ is porosity, and Λ is the thermal expansion coefficient of the fluid. The variable R_t represents the chemical transformation ratio between kerogen and oil, and ρ_s, ρ_k and ρ_{oil} are densities of solid, kerogen and oil, respectively. By these relationships, changes in pore fluid pressure can be created by changes of total vertical stress by the sediment loading (σ_v), by creation of liquid petroleum, and by changes in subsurface temperature (T).

Assuming Athy's Law behavior (Athy, 1930; Bethke and Corbet, 1988), the initial porosity (ϕ_0) diminishes by increasing effective stress (that is, increasing sediment loading) until it reaches an irreducible limit (ϕ_{ir}) (Person and Garven, 1994)

$$\phi = \phi_0 \exp\left(\frac{-\beta_v \sigma_e}{g(\rho_s - \rho_f)}\right) + \phi_{ir} \tag{4}$$

where β_v is the vertical bulk compressibility of the medium, and σ_e is the effective stress by the compaction. The permeability of compacting sediments is generally assumed to track directly with changes in porosity, and many researchers have adopted a log-linear correlation (for example Bethke, 1985)

$$\log k = C\phi + D \tag{5}$$

where C and D are log-linear empirical fitting parameters based on data sets.

The governing equation for heat transport is derived from conservation of thermal energy (per unit volume), and includes both conductive and convective heat transport (Bethke, 1985)

$$[c_f \rho_f \phi + c_s \rho_s (1 - \phi)]\frac{\partial T}{\partial t} = -\nabla \cdot (\lambda^* \nabla T) + \rho_f c_f \mathbf{q} \nabla T + \frac{\rho_f h_f}{(1 - \phi)}\frac{\partial \phi}{\partial t} \tag{6}$$

where c_f and c_s are the specific heat capacity of fluid and solid, $\boldsymbol{\lambda}^*$ is thermal dispersivity tensor, and h_f is fluid enthalpy. The thermal dispersivity is proportional to the fluid flux, and it can be expressed in combination of longitudinal and transverse dispersivities and thermal conductivities of fluid and solid (Bear, 1972)

$$\lambda_{xx} = \rho_f c_f \frac{q_x^2}{|\mathbf{q}|}\alpha_L + \rho_f c_f \frac{q_z^2}{|\mathbf{q}|}\alpha_T + \lambda_f^{\phi}\lambda_s^{1-\phi} \tag{7}$$

$$\lambda_{zz} = \rho_f c_f \frac{q_z^2}{|\mathbf{q}|}\alpha_L + \rho_f c_f \frac{q_x^2}{|\mathbf{q}|}\alpha_T + \lambda_f^{\phi}\lambda_s^{1-\phi} \tag{8}$$

$$\lambda_{xz} = \lambda_{zx} = \rho_f c_f \frac{q_x q_z}{|\mathbf{q}|}(\alpha_L - \alpha_T) \tag{9}$$

where λ_{ij} and q_i are 2-D components of thermal dispersivity and Darcy flux, and α_L and α_T are longitudinal and transverse fluid dispersivities. Thermal conduction tends to dominant heat transport in sedimentary basins.

RIFT2D uses a standard Galerkin finite element method for solving the coupled equations of fluid flow and heat transport. The model can simulate fluid flow due to sediment compaction, fluid density variations, effects of topography, and additional effects of fluid pressure related to petroleum generation. For details on the methods used in the numerical scheme, see Person and Garven (1994).

Petroleum maturation can be approximated in a simplified sense as a first-order, thermally-controlled kinetic reaction model (Tissot and others, 1986, 1987) and used to predict spatial distribution of the matured petroleum mass. Kerogen is an insoluble organic compound composed primarily of C-O, H-O and H-C chemical bonds. In order to break these chemical bonds, variable amounts of energy are required. This energy is referred to as the activation energy. The rate of petroleum generation at a certain temperature can be expressed by a first-order kinetic equation:

$$\frac{dx_i}{dt} = -K_i x_i \tag{10}$$

where x_i is the petroleum potential of kerogen involved in reaction i, and K_i is the Arrhenius constant for the i-th reaction related with the absolute temperature (T) and the activation energy (E_i),

$$K_i = A_i \exp\left(-\frac{E_i}{RT}\right) \tag{11}$$

where A is the pre-exponential coefficient and R is the gas constant. The range of Arrhenius constant (K_i) values for the Monterey Formation is 1.42×10^{-15} to 2.78×10^{-13}/s (Jarvie and Lundell, 2001). The calculated petroleum mass converted into kerogen defines the transformation rate (R_t), which contributes to an increase in the fluid pressure. Once the mass of generated petroleum is calculated from the kinetic equation, then petroleum saturation can be determined by dividing the total petroleum volume by the effective sediment porosity of the sediment. The calculated petroleum saturation distribution is used to constrain the boundary condition of the multiphase petroleum migration model.

Model I Setup

The numerical grid for the final structural stage of the compaction model (fig. 6) is based on the structural interpretation of seismic images by Shaw and Suppe (1996). The simulations are spatially limited to the western part of the Los Angeles basin that contains the southwestern block and the western half of the central syncline. The basin profile orientation from the southwest to the central block was chosen for the numerical simulations because this region is known for many oil fields that are associated with regional fault structures (for example NIFZ) and it is also the primary interest to elucidate the role of the fault on the formation of those reservoirs. The time frame of Los Angeles basin compaction model is set from the mid-Miocene (~14 Ma) to the present because most of the basin consists of Miocene to Pleistocene sediments resting on much older crystalline rocks (for example Catalina Schist). The crustal deformation since the late Pliocene that caused the uplift of the San Gabriel Moun-

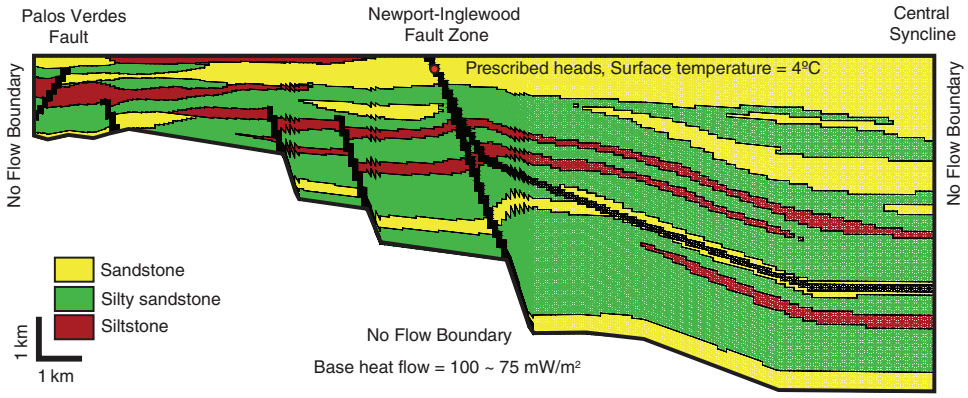

Fig. 6. The numerical grid (120 columns and 40 rows) and hydrostratigraphy, and boundary conditions used in the LA basin compaction model.

tains on the eastern side of the basin is also considered in the model because this deformation phase influences the regional groundwater flow significantly.

Formation water total dissolved solids (TDS) in Los Angeles basin area does not exceed seawater salinity and usually ranges 20,000 to 34,000 ppm (Hesson and Olilang, 1990; California Department of Conservation, 1992) for most oil reservoirs. We set water salinity to 25,000 ppm (mg/L) for the model based on those observed data. The sedimentary rocks are assumed to be fully saturated and the upper boundary is treated as a prescribed pressure condition. The boundary pressure values are then changed from the height of sea level to the land surface elevation after uplift of the basin began. The top temperature is assigned as a constant value of 4 °C throughout the simulation time, assuming that deep sea temperature was not significantly affected by climate change. The left and bottom of the domain are treated as no-flow-boundary because they represent the crystalline basement rocks having much lower permeability. The right side of the domain is the center of the basin that is assumed to be a hydraulic divide, so the no-flow boundary condition is assigned.

Hayba and Bethke (1995) argued that heat flux into the basin floor should be as high as 2.0 HFU (~100 mW/m^2) in middle Miocene time and gradually decreased to 1.5 HFU to better match the suggested oil window depth proposed by Jeffrey and others (1991). We set the basement heat flux linearly decreased from 100 to 75 mW/m^2 during burial, considering the high temperature environment of the active basin in the early Miocene, characterized by frequent volcanic and plutonic extrusion/intrusion events (Wright, 1991; McCulloh and others, 2000; Bilodeau and others, 2007). The field observation also indicates the average heat flux today in the Los Angeles basin region is about 73 mW/m^2 (Sass and others 1971; Williams and others, 2001).

Based on the borehole logging data, sedimentary rocks in the Los Angeles basin were grouped into three major hydrogeologic units: sandstone, silty sandstone, and siltstone (fig. 2). The representative hydrogeologic parameters assigned to each unit are presented in table 2. These parameters were chosen from publications dealing with field and experimental tests on the aquifers in this region. Permeability data of the deep basement rocks are rare and hard to obtain; however, a few wells in relatively shallow Pleistocene and upper Pliocene rocks, mostly consisting of sandstone and silty sandstone, were hydrologically tested. The United States Geological Survey conducted slug tests at wells in the central and west coast of the Los Angeles basin and estimated

TABLE 2

Parameters used in the LA basin compaction model

	Sandstone	Silty sandstone	Siltstone	Fault
Permeability fitting coefficient, C	-16.0	-16.5	-17.0	-14.5
Permeability fitting coefficient, D	7.0	6.0	5.0	7.0
Anisotropic ratio, k_x/k_z	10.0	10.0	10.0	1.0
Initial porosity, ϕ_0	0.35	0.38	0.55	0.45
Irreducible porosity, ϕ_{ir}	0.05	0.05	0.05	0.05
Fitting parameter for sediment compressibility, B_s (m^{-1})	5.5×10^{-3}	6.0×10^{-3}	6.5×10^{-3}	0.05
Thermal conductivity, λ (W/m°C)	2.0	1.8	1.5	2.0
TOC (%)	4.0	4.0	16.0	4.0
Petroleum type (%) (Type I: Type II: Type III)	40:50:10	45:50:05	50:50:00	50:50:00

hydraulic conductivities (K) that can be converted to permeabilities (k) ranging from 1.1×10^{-12} to 2.5×10^{-12} m^2 (1100- 2500 md) in the Pleistocene aquifer (for example San Pedro formation) and 3.5×10^{-14} to 2.8×10^{-12} m^2 (35–2800 md) in the Pliocene aquifer (for example Pico formation) (Reichard and others, 2003; Nishikawa and others, 2009). They also analyzed core samples taken from sediment predominantly consisting of clay, silt, and sand; the permeabilities from these cores were 1.38×10^{-15}, 3.53×10^{-15}, and 3.53×10^{-14} m^2 (1.38, 3.53, and 35.3 md), respectively. Higgins and Chapman (1984) also reported that the permeability of upper Miocene sediments in the Seal Beach oil field was in the range of 2.0×10^{-14} to 1.5×10^{-13} m^2 (20–150 md) and the porosity and permeability significantly decreased with depth. Field observed hydrogeologic properties for selected locations are organized in table 3.

The permeability of each unit depends on effective stress and is calculated using an empirical porosity-permeability-depth relationship (eqs. 4 and 5). The permeability-porosity correlations for each rock type are illustrated in figure 7. The permeability of

TABLE 3

Hydrogeologic data of LA basin

Formation	Age	Location	Depth (km)	Porosity (%)	Permeability (md)	Average Permeability (m^2)	TDS (ppm)	Oil Density (kg/m^3)	Reference
Puente	U Miocene	Long Beach	0.91	32-35	700	7.00E-13	32600	936.2	(1)
Puente	U Miocene	Long Beach	1.06		450-500	4.75E-13	32000	900.4	(1)
Puente	U Miocene	Long Beach	1.21		150-190	1.70E-13	34200	883.5	(1)
Puente	U Miocene	Long Beach	1.37		100	1.00E-13	25700	875.3	(1)
Puente	U Miocene	Long Beach	1.67		275	2.75E-13	23900	875.3	(1)
Puente	U Miocene	Seal Beach	2.04	21-24	50-150	1.00E-13	23000	878.0	(1)
Puente	U Miocene	Seal Beach	2.49	16-1	20	2.00E-14	31000	875.3	(1)
Puente	U Miocene	Seal Beach	1.58	21	36				(2)
Puente	U Miocene	Seal Beach	1.90	21	36				(2)
Puente	U Miocene	Seal Beach	2.43	15	20				(2)
Repetto	L Pliocene	Long Beach	0.67	30-40	1000-1600	1.30E-12	28000	974.9	(1)
Repetto	L Pliocene	Long Beach	0.76		700-1600	1.15E-12	31700	942.4	(1)
Repetto	L Pliocene	Seal Beach	1.60				31600	912.0	(1)
Repetto	L Pliocene	Seal Beach	1.64	28-37	200	2.00E-13	31000	915.0	(1)
Repetto	L Pliocene	Seal Beach	1.70	29-30	400-600	5.00E-13	27000	897.5	(1)
Repetto	L Pliocene	Seal Beach	1.77	24-28	125-1281	7.03E-13	28350	909.0	(1)
Schist	Cretaceous	Long Beach	1.79		<500	3.00E-13	17100	875.3	(1)

1) Higgins and Chapman, 1984; (2) Hesson and Olilang, 1990.

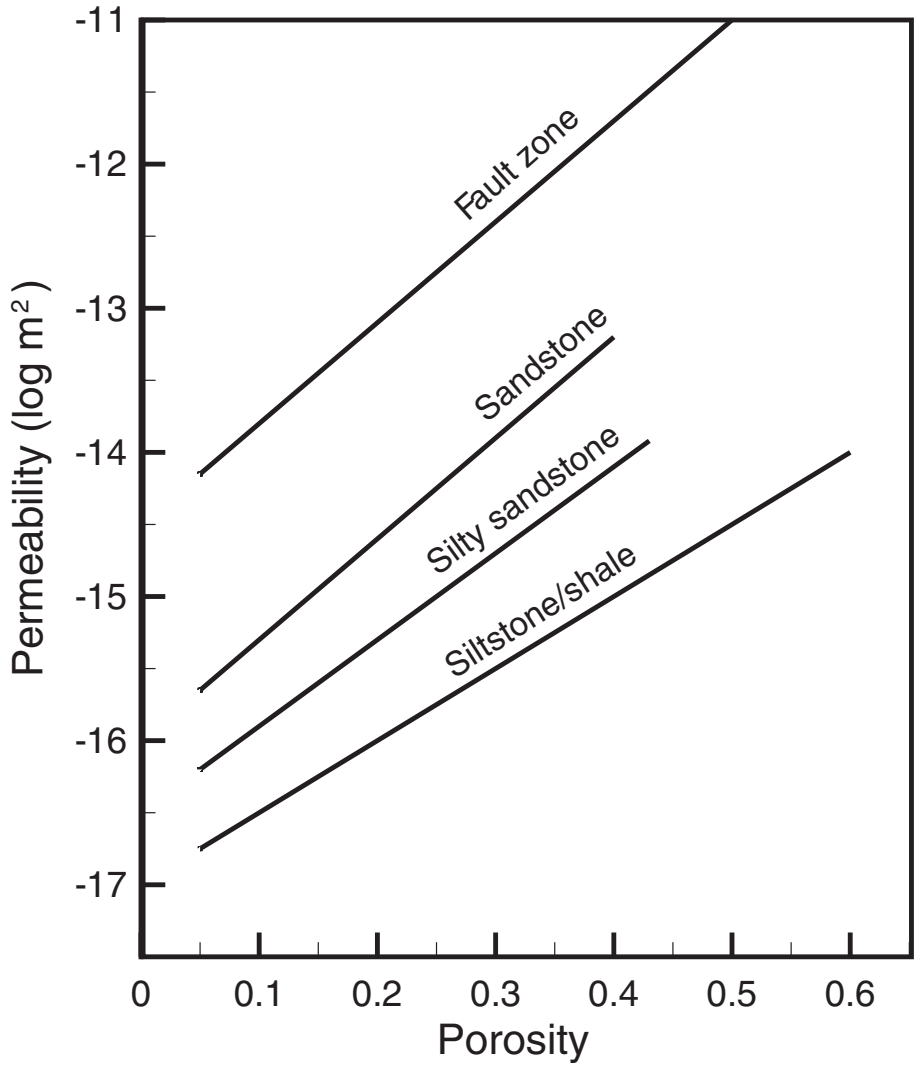

Fig. 7. Assumed porosity-permeability relations for model sediments in the LA basin. Data adopted from Corbet and Bethke (1992) and Mercer and others (1982).

unconsolidated sandstone is greater than 300 md at the depositional surface, and it was gradually decreased downward to less than 3 md. The hydraulic conductivities of silty sandstone and siltstone are set to smaller than that of sandstone due to their higher contents of silt and clay. Higher medium compressibility (β_v) is also assigned to these rocks because the compaction rate of clay-rich sediment is much higher than other strata.

The upper Miocene sequences were deposited in marine environments and contain the most significant amount of organic matter for petroleum generation. All of these formations are composed of shallow marine sediments and have rich organic compounds (Redin, 1991; Kaplan and others, 2000). We set TOC = 16 percent for siltstone layers because these fine grain sediments with high shale contents typically

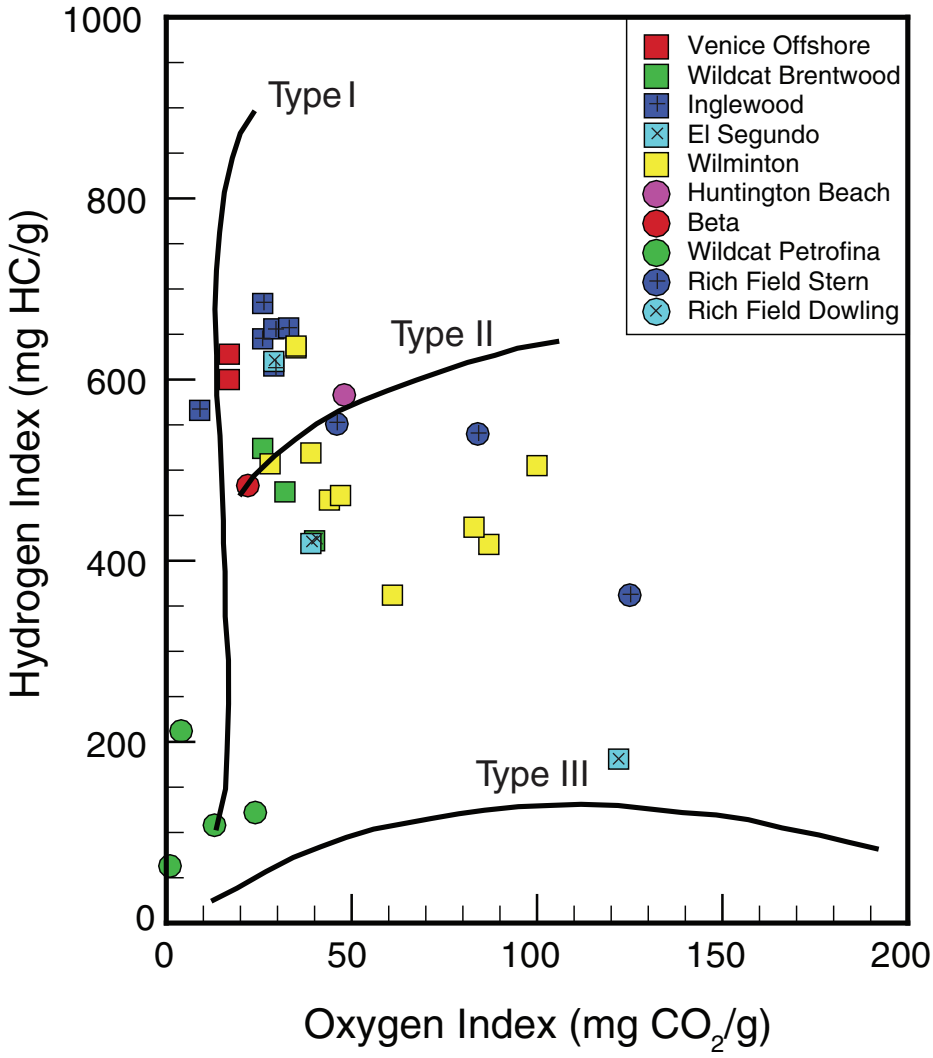

Fig. 8. Modified van Krevelen diagram showing kerogen types of LA basin oils and source rocks (data from Kaplan and others, 2000).

contain more abundant organic materials. Furthermore, TOC = 4 percent for other types of rocks that are not considered main source rocks. For example, the TOC content of the Puente Formation ranges up to 16 percent but averages 4 percent, and that of the Monterey Formation is in the range of 2 to 18 percent. TOC contents in upper Miocene rocks are very high compared to other strata, and these are considered as a primary hydrocarbon source (Jeffrey and others, 1991). As shown in the modified van Krevelen diagram (fig. 8), kerogen types analyzed from oil and source rock samples can be categorized in Type I and Type II, which have hydrogen-rich and oxygen-poor organic compounds from the marine sources. These types of kerogens tend to produce more oil than gas or coal. We set the composition of kerogen type in siltstone as 50%: 50%: 0% (Type I: Type II: Type III) and sandstone as 40%: 50%: 10%,

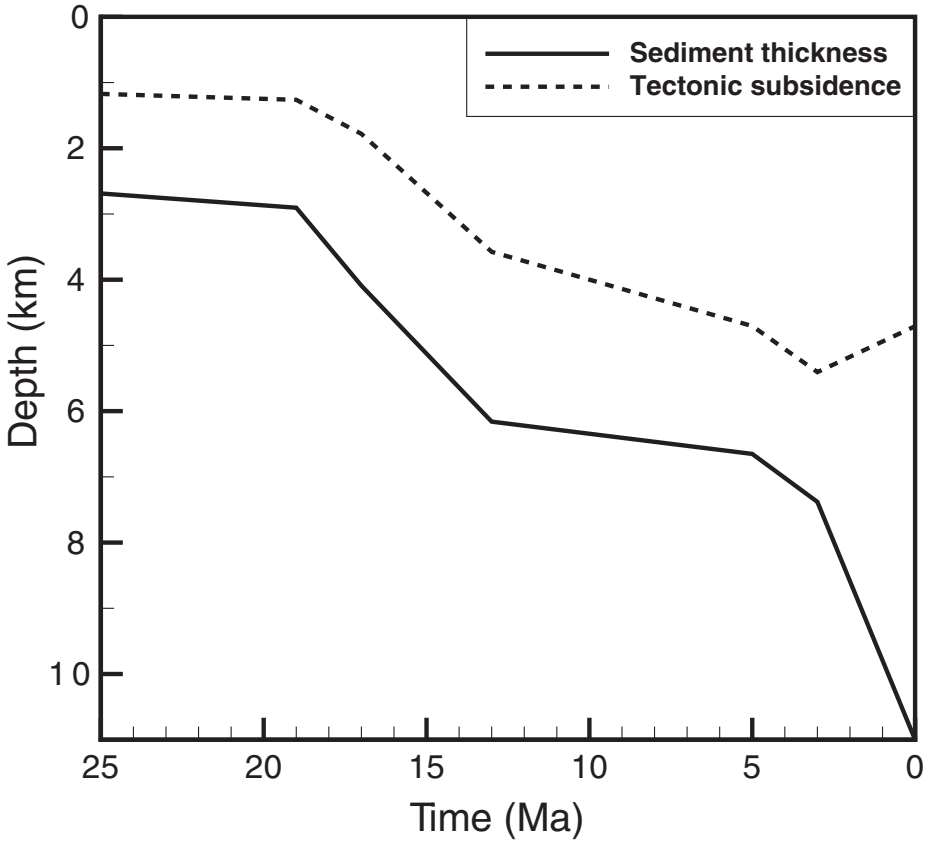

Fig. 9. Subsidence history of the central block of the LA basin (after Mayer, 1991).

considering that the woody and vegetal components in kerogens generally increased in coarse continental sediments.

Tectonic subsidence rates for a basin can be estimated from geochronologic geohistory analysis and a backstripping method (Steckler and Watts, 1978; van Hinte, 1978). This procedure reconstructs the density structure of a sedimentary column that can eventually be converted into the sediment thickness and tectonic subsidence rate. We adopt the tectonic subsidence data from the geohistory plot by Mayer (1991) (fig. 9) and use it for the compaction model. According to his plot, the basin bottom starts to subsidize from about 18 Ma and continues to drop until 13 Ma at a relatively constant rate, after which the subsidence stops until it drops again at 5 Ma. This pattern of subsidence approximately corresponds to NW-SE tectonic extension that occurred in the Miocene (fig. 3). After 3 Ma, the sediment thickness increases at a faster rate, but the depth of basin bottom slightly rises by tectonic uplifting, a process related to the late Pliocene-Pleistocene deformation. The timing of this change matched the results of another geohistory analysis independently performed by Saywer and others (1987). The sediment thickness generally increases with increasing subsidence even during the uplift, probably due to the massive influx of continental sediments from the newly elevated San Gabriel Mountains region. Tectonic subsidence rates at selected locations used in the model are listed in table 4. The subsidence rates are generally high in the central syncline and gradually decrease towards the western basin

TABLE 4

Tectonic subsidence/uplift rates for compaction model

Period (Ma)	Subsidence/ Uplift Rate (mm/yr)		
	Central Syncline	Newport-Inglewood Fault Zone	Palos Verdes Peninsula
13.8-9.8	0.876	0.500	0.190
9.8-3.5	0.857	0.488	0.186
3.5-1.0	0.574	0.329	0.125
1.0-Present	-0.051 (Uplift)	0.000	-0.025 (Uplift)

margin in the Palos Verdes region. We set the top surface of model to be elevated after 1 Ma, assuming the topography of the basin would begin to change, after tectonism completely entered into the compressional regime (fig. 3). We assume that the deep thrust fault zone in the center was activated during the uplift, so rock properties assigned to these elements are also changed to the same values with the fault zone after 1 Ma.

Model I Results

Overpressure starts to accumulate in the Miocene sediments immediately after the subsidence begins (fig. 10A). Computed overpressures (hydraulic heads) reached a maximum at the end of the Pliocene to Pleistocene (~1.5 Ma) when the upper Miocene formation is compacted by continuous tectonic subsidence and sediment loading (fig. 10B). Overpressured zones mostly appear in the central basin and the geopressure pattern seems to follow the trend of siltstone layers because of their high compressibility and fast burial rates in the center. The computed hydraulic head difference between the sea floor and the maximum pressure zone at the central syncline is about 200 m, and these excessive pore pressures may contribute to driving forces for groundwater and petroleum migration in the basin. The overpressure decreased after the compaction of Miocene sediments reached the maximum and began to dissipate pore pressure into more permeable Pliocene formations during the subsidence in progress.

Late Pliocene-Pleistocene deformation altered land-surface topography, uplifting both the eastern side (San Gabriel Mountains) and the western side (Palos Verdes Peninsula) of the basin. This physiographic change of land surface affects the regional groundwater flow pattern. Before the deformation, the groundwater flow was solely compaction-driven and moved from the overpressured upper Miocene formation to the surface through the fault and aquifer flow channels. However, at present, the topographically-driven regional groundwater flow dominates the uplifted basin after deformation (fig. 10C). According to the regional groundwater flow model constructed by the USGS (Reichard and others, 2003), hydraulic potential follows land elevations, which are high in Palos Verdes, Santa Monica, and San Gabriel Mountain regions and low in the central basin. The measured hydraulic head difference between the Palos Verdes Peninsula and the central basin was approximately 40 to 80 m. Although these data were obtained from shallow aquifers, the overall flow pattern agrees with that of the simulated present hydraulic conditions of our model.

During the first extension in the middle Miocene (~13 Ma), groundwater flowed from the basin center to fault zones and western borderlands. The primary driving force at this period was sediment compaction, but the flow rate was relatively small because the loaded sediments are less compressible sandy materials (fig. 11A). A high

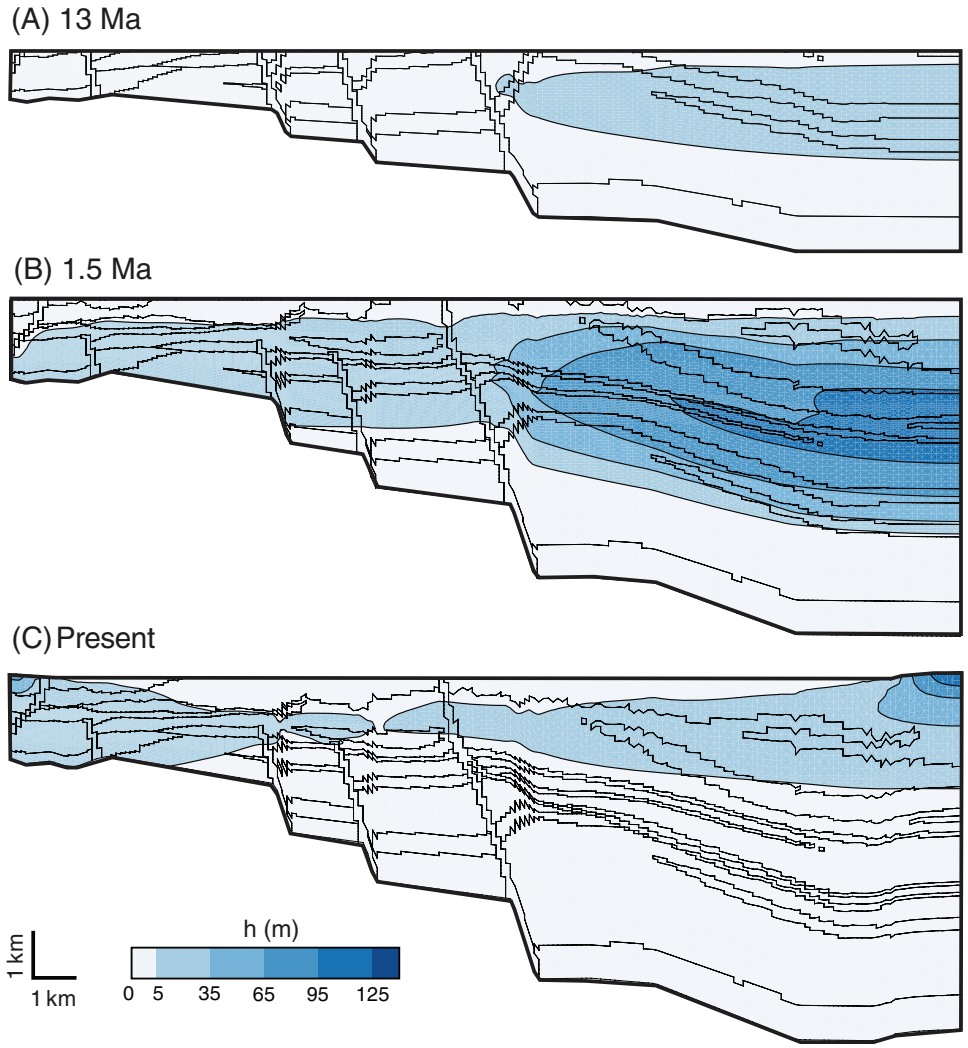

Fig. 10. Modeled fluid potential change (Δh) within the LA basin. Note that there are topographic changes by uplifting on the upper surface.

velocity zone was focused on the Newport-Inglewood fault zone and the lower sandstone layer. The compaction-driven groundwater flow is intensified during the second stage of tectonic extension that occurred in the late Miocene-Pliocene due to the increased subsidence rate and the burial of highly compressible siltstone layers. At about 1.5 Ma, groundwater velocity in the upper part of the NIFZ reached ~2.0 m/yr (fig. 11B). During the late Pliocene deformation, N-S trending transpressional forces elevated the topographic surface of the basin edges, and consequently the groundwater flow system gradually converted from the compaction-driven to dominantly topographically-driven regime. Therefore, at present, forced groundwater circulations form both western and eastern sides of the basin are dominant, and the flow rate in the NIFZ is comparatively weakened as the overpressure in the sediments has dissipated (fig. 11C). Also, relatively high velocity is detected in the central thrust fault zone by the deformation-triggered reactivation.

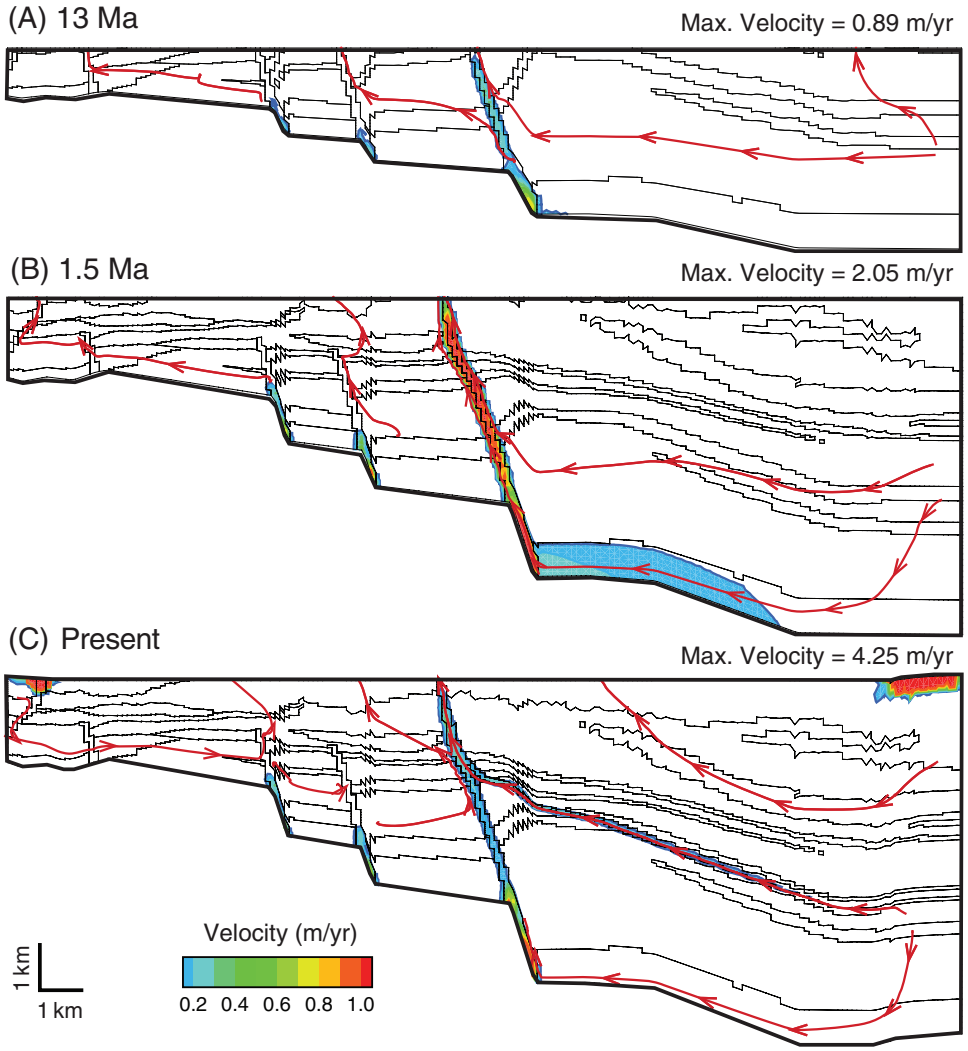

Fig. 11. Groundwater velocities within the LA basin. The white-colored areas indicate where fluid velocity is less than 0.1 m/yr, and the red arrows represent selected fluid paths within the basin.

Temperature profiles obtained from the compaction model are dominated by conductive heat transport, and the contour lines are mostly parallel to the basin surface except for slightly elevated temperature in the NIFZ (fig. 12A). The temperature anomaly in the fault zone is probably due to the compaction-driven flow from the center. Temperature in the NIFZ is elevated considerably when the compaction reaches the maximum in the late Pliocene because of the heat (energy) convected by the focused groundwater flow in the fault zone (fig. 12B). At present, the temperature anomaly is weakened due to the overall temperature increase across the basin and reduced groundwater flow in the fault zone (fig. 11C). The temperature fluctuation in the fault zone is closely related to the groundwater velocity (fig. 13). Both velocity and temperature have the highest values during the second tectonic extension period in the late Miocene to Pliocene, and drop later by the uplift and the weakened compaction-driven flow.

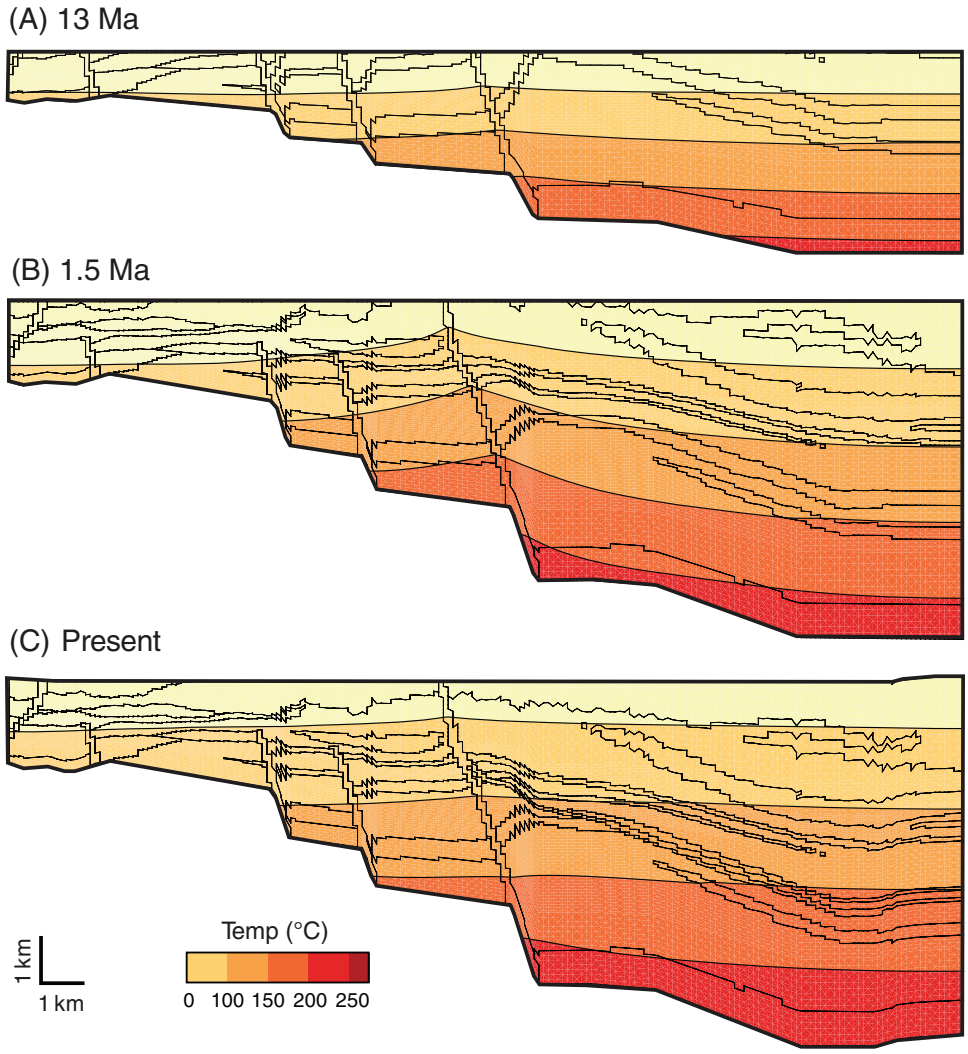

Fig. 12. Evolution of temperature in the LA basin.

The computed geothermal gradient in the NIFZ obtained from the compaction model (a red line with circles) is compared with field observations at various locations in the Los Angeles basin (fig. 14). The geothermal gradient in the NIFZ is approximately 3.5 °C/100 m and the present geothermal gradients in other places are in the range of 3.0 to 4.0 °C/100 m (data obtained from McCulloh, 1979). The highest gradients appear along the southwestern and northern margins, while the lowest gradient is shown in the central syncline. These data are consistent with other observations (Bostick and others, 1978) that confirm the trend of increasing geothermal gradient from the basin center to the margins. Higgins and Chapman (1984) also determined the geothermal gradient to be in the range of 3.5 to 4.04 °C/100m from the wells near NIFZ (the Seal Beach Naval Weapons Station). The computed temperature profile is in agreement with observational profiles within a small range of

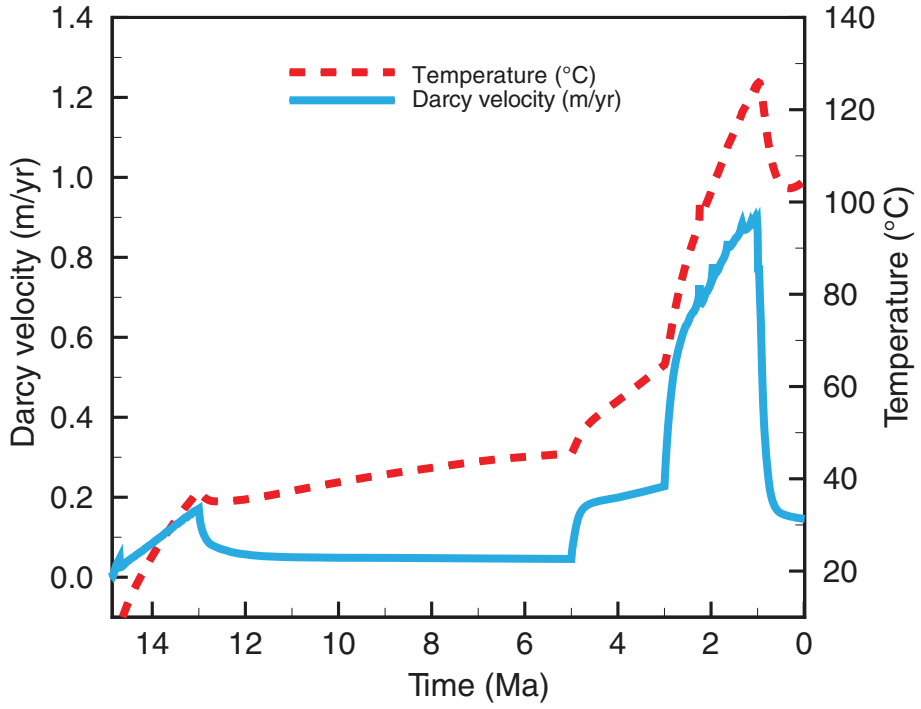

Fig. 13. Evolution of groundwater specific discharge and temperature in the fault zone (marked as a red circle in fig. 6).

difference, especially one from the Long Beach field in NIFZ (a blue line with square), although there is a lack of measured data to compare below 5 km.

Computed petroleum generation from the middle Miocene to the present is illustrated in figure 15. According to the simulation results, the matured petroleum source zone (also known as the "oil window") is apparent within a depth range of 4 to 6 km in the central basin. The depth of this zone is slightly elevated in the NIFZ because it basically follows temperature distribution that is enhanced by convective heat flux. The potential petroleum producing area increases with temperature and burial time. In the present distribution, the productive zone extends far to the west and also contains the deep part of the NIFZ. Modeled petroleum producing potential is high in siltstone layers because of high TOC that can be converted into petroleum. The petroleum mass (milligrams) can be calculated from a unit mass (gram) of source rock. The range is 30 to 90 mg/g for siltstone layers and 20 to 40 mg/g for sandstone and silty sandstone layers within the matured zone (fig. 15C). The organic materials would decompose into lighter hydrocarbon compounds (for example, methane) and carbon dioxide, if the source depth were below this zone.

The temporal variation of the accumulated total petroleum volume generated from the source zone is plotted in figure 16. The modeling results show that petroleum generation mainly occurred during the middle Miocene (16-12 Ma) and after the Pliocene (5-0 Ma), and the timing of massive oil production was closely related to the tectonic extension events in the basin. Within the relatively short period of geologic time (~2 My), petroleum generation in the second stage of tectonic extension

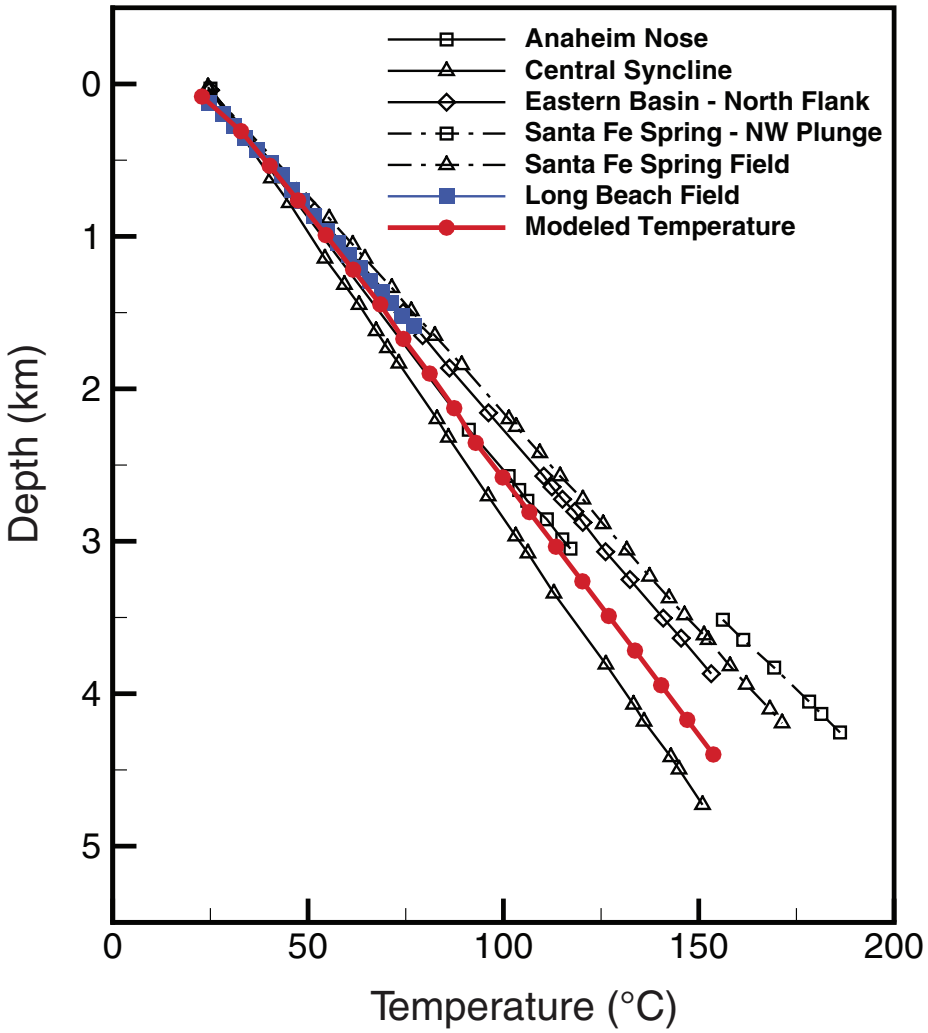

Fig. 14. Observed and modeled temperature profiles along the depth (McCulloh, 1979). Modeled profile is obtained from the Newport-Inglewood fault zone.

accumulates over 50 percent of the total oil volume stored in the basin and likely continues to the present.

PETROLEUM MIGRATION IN THE LA BASIN

Petroleum Migration Model (Model II)

The sediment compaction model is an effective way to understand the regional evolution of geopressures in a basin, but it cannot explicitly deal with the petroleum migration problem, which needs the physics of separate phase fluid flow. We develop below a multiphase fluid flow model based on the results from the compaction model. The multiphase flow model used in this study only considers water and oil phases and neglects the presence of petroleum gas, as a first approximation.

There are many schemes used for formulating the multiphase flow phenomena, but here we derive a decoupled formulation based on fluid pressure and saturation.

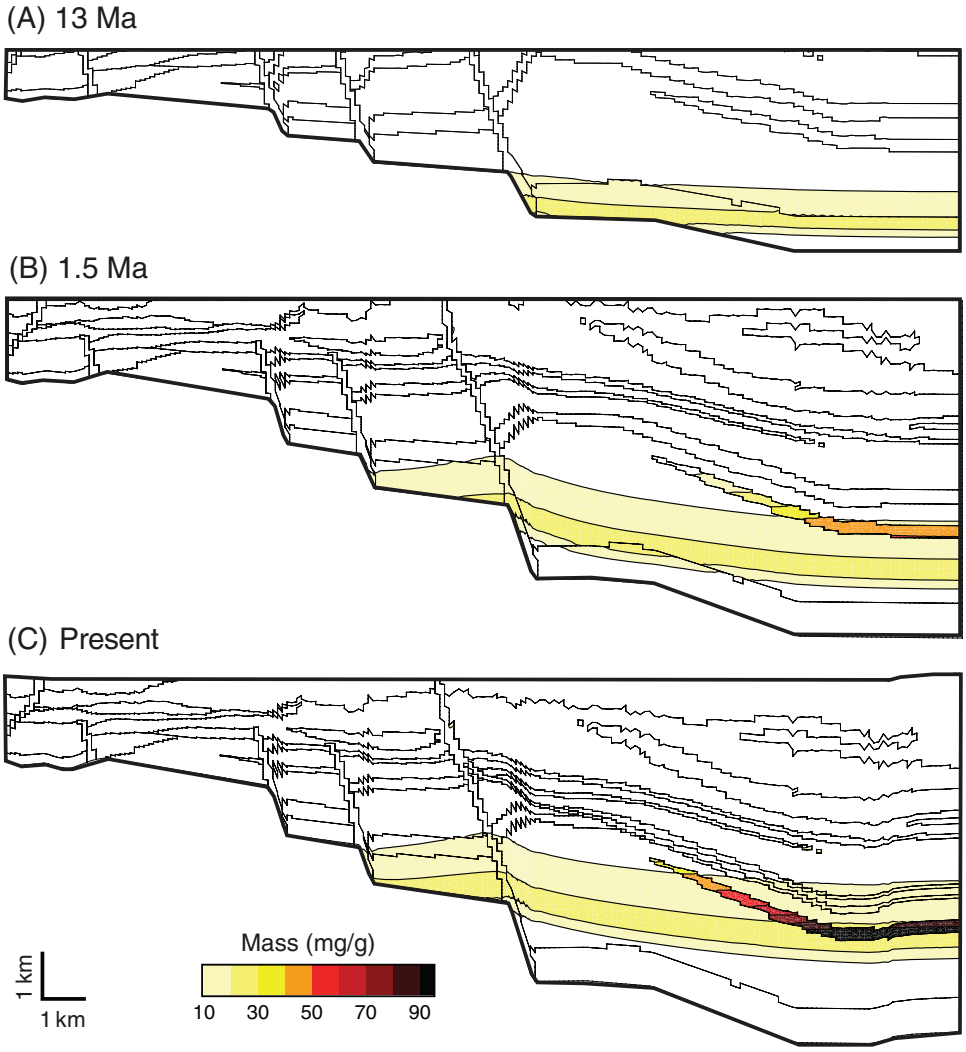

Fig. 15. Distribution of petroleum generation potential (in mg/g source rock).

For a two-phase system, the conservation of mass for each phase can be written as (Forsyth and Wasow, 1960; Scheidegger, 1960; Pinder and Gray, 1977; Aziz and Settari, 1979; Tóth, 1987; Pruess, 1991; Helmig, 1997; Geiger and others, 2004; Chen and others, 2006):

Phase 1: wetting phase (for example water)

$$\phi \frac{\partial(\rho_w S_w)}{\partial t} = -\nabla \cdot (\rho_w \mathbf{v_w}) + \rho_w m_w \tag{12}$$

Phase 2: non-wetting phase (for example liquid petroleum)

$$\phi \frac{\partial(\rho_n S_n)}{\partial t} = \phi \frac{\partial(\rho_n (1 - S_w))}{\partial t} = -\nabla \cdot (\rho_n \mathbf{v_n}) + \rho_n m_n \tag{13}$$

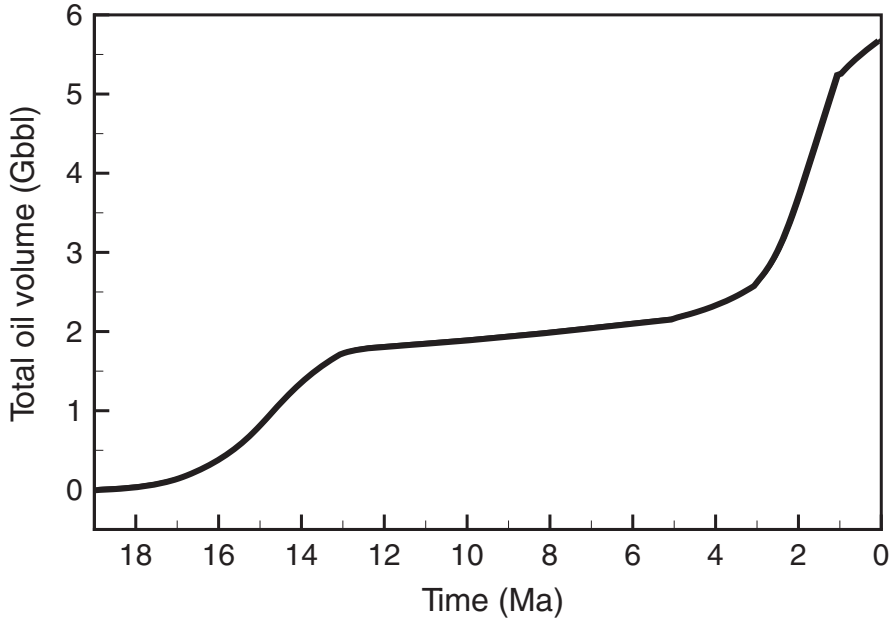

Fig. 16. Cumulative oil volume generated in the LA basin, as predicted by the sediment-compaction model.

where S is the saturation and the subscripts n and w denote the non-wetting and wetting phases, respectively, and m represents the internal rate of mass accumulation or depletion per unit volume (source/sink term). Constant porosity, low Reynolds Number flow (Darcy flow), and slightly compressible fluids are assumed in the equations.

Summing up equations for both phases (eqs. 12 and 13) and introducing the total fluid flux of the two-phase system ($\mathbf{v_t}$), the gradient of this term can be defined as

$$\nabla \cdot \mathbf{v_t} = \nabla \cdot (\mathbf{v_w} + \mathbf{v_n}) = -\frac{1}{\rho w}\mathbf{v_w} \cdot \nabla \rho_w - \frac{1}{\rho_n}\mathbf{v_n} \cdot \nabla \rho_n + m_w + m_n + \phi\left(\frac{S_w}{\rho_w}\frac{\partial \rho_w}{\partial t} + \frac{S_n}{\rho_n}\frac{\partial \rho_n}{\partial t}\right) \quad (14)$$

If both phases are incompressible, equation 15 becomes

$$\nabla \cdot \mathbf{v_t} = m_w + m_n = 0 \quad (15)$$

If the fluids are, however, slightly compressible, the derivative terms in equation 14 can be equated to the total compressibility of the medium (c_t) and a time derivative of an average pressure of fluids (Huber and Helmig, 1999, 2000; Geiger and others, 2004) is given by

$$\phi c_t \frac{\partial \bar{P}}{\partial t} = \phi\left(\frac{S_w}{\rho_w}\frac{\partial \rho_w}{\partial t} + \frac{S_n}{\rho_n}\frac{\partial \rho_n}{\partial t}\right) + \frac{\nabla \rho_w}{\rho_w} \cdot \mathbf{v_w} + \frac{\nabla \rho_n}{\rho_n} \cdot \mathbf{v_n} = -\nabla \cdot \mathbf{v_t} + m_t \quad (16)$$

where c_t is the total bulk compressibility of the medium, and q_t is a total source/sink term. By definition, $\bar{P}$ is the arithmetic average of water and oil pressure and related to capillary pressure (p_c),

$$\bar{P} = \frac{1}{2}(p_w + p_n) = p_w + \frac{1}{2}p_c = p_n - \frac{1}{2}p_c \tag{17}$$

The Darcy fluxes for wetting and non-wetting fluids can be expressed according to Darcy's law (conservation of linear momentum):

$$\mathbf{v_w} = -\lambda_w \mathbf{k}(\nabla p_w - \rho_w \mathbf{g}) \tag{18}$$

$$\mathbf{v_n} = -\lambda_n \mathbf{k}(\nabla p_n - \rho_n \mathbf{g}) = -\lambda_n(\nabla p_w + \nabla p_c - \rho_n \mathbf{g}) \tag{19}$$

where $\mathbf{g} = (0, 0, -g)$ and the fluid mobility coefficients are

$$\lambda_w = \frac{k_{rw}}{\mu_w};\ \lambda_n = \frac{k_{rn}}{\mu_n} \tag{20}$$

The total fluid flux term ($\mathbf{v_t}$) can be derived by adding fluxes from two phases

$$\mathbf{v_t} = \mathbf{v_w} + \mathbf{v_n} = -\mathbf{k}\{\lambda_t \nabla \bar{P} - 0.5(\lambda_w - \lambda_n)\nabla P_c - (\lambda_w \rho_w + \lambda_n \rho_n)\mathbf{g}\} \tag{21}$$

where the total mobility coefficient $\lambda_t = \lambda_w + \lambda_n$. Substituting equations 18 and 19 into 16, one obtains a decoupled form of the pressure equation (Helmig, 1997; Geiger and others, 2004)

$$\phi c_t \frac{\partial \bar{P}}{\partial t} = -\nabla \cdot \mathbf{v_t} + q_t = \nabla \cdot \mathbf{k}\{\lambda_t \nabla \bar{P} - 0.5(\lambda_w - \lambda_n)\nabla p_c - (\lambda_w \rho_w + \lambda_n \rho_n)\mathbf{g}\} + m_t \tag{22}$$

But further algebraic manipulation is needed to obtain a decoupled saturation equation. The non-wetting phase flux ($\mathbf{v_n}$) can be rewritten in terms of total fluid flux ($\mathbf{v_t}$) and the capillary pressure (p_c)

$$\mathbf{v_n} = \frac{\lambda_w}{\lambda_t}\mathbf{v_t} - \frac{\lambda_w \lambda_n}{\lambda_t}\mathbf{k}\{\nabla p_c + (\rho_w - \rho_n)\mathbf{g}\} \tag{23}$$

Equation 23 can be simplified further using fractional flow coefficients, which are defined as

$$f_w = \frac{\lambda_w}{\lambda_t};\ f_n = \frac{\lambda_n}{\lambda_t};\ \bar{\lambda} = \frac{\lambda_w \lambda_n}{\lambda_t} \tag{24}$$

Substituting equation 23 into 13, one gets the final working form of the saturation equation,

$$\phi \frac{\partial S_n}{\partial t} + \nabla \cdot [f_n \mathbf{v_t} - \bar{\lambda}\mathbf{k}\{\nabla p_c + (\rho_w - \rho_n)\mathbf{g}\}] - m_t = 0 \tag{25}$$

which is decoupled from the original pressure-saturation formulation. This transformation provides a basis for a robust numerical formulation of the governing equations by adopting the implicit pressure-explicit saturation (IMPES) technique.

Numerical Formulation

Combined finite element and finite volume methods (FEFVM) with the IMPES formulation provide a good alternative for traditional fully-coupled direct solution methods (Durlofsky, 1993, 1994; Chen and others, 2006). The IMPES scheme allows one to avoid computationally-expensive iterative nonlinear solution algorithms, such

as Newton's method. Each equation can be solved separately and feeds back through the shared fluid velocity and saturation terms.

Another advantage of the IMPES method is the possibility of combining merits from both finite element and finite volume methods (Geiger and others, 2004). The geometric flexibility of the finite element method (FEM) allows one to obtain the flow field in complex geological settings. In addition, the saturation equation can be solved more effectively by using the finite volume method (FVM). The FVM method particularly offers a better solution for the mass conservation problem under hydrogeologic settings that often produce non-realistic results, such as formation boundaries having a high permeability contrast (Durlofsky, 1993, 1994). Furthermore, the numerical efficiency of matrix operations and algebra can also be achieved by decoupling and by making the matrices positive definite and diagonally dominant.

For the petroleum migration model presented in this paper, we developed a new program called TUFTS-FV that uses the standard Galerkin finite element method coupled with an implicit time scheme for the fluid pressure equation, and the finite volume method with explicit time for the fluid saturation equation.

Both the finite element and finite volume algorithms are well documented in various textbook sources [for example (Zienkiewicz, 1977; Chen and others, 2006)] hence, only a summary description will be provided here. If the pressure equation is spatially discretized by linear interpolation functions, the pressure

$$\bar{P}(\mathbf{x},t) = \sum_{j}^{N} \bar{P}_j \xi_j(\mathbf{x}),\ \mathbf{x} \in R \tag{26}$$

where $\bar{P}_j$ is the average pressure (Galerkin coefficient) at the node j, and ξ_j is the basis or shape function at the node j that varies linearly between neighboring nodes, being 1 at the node j and zero at all other nodes, and N is the total number of nodes in a mesh domain defined in R. According to the Galerkin FEM, one must find the optimal coefficients that minimize the following integrals with weighted residuals:

$$\int_R \Upsilon(\bar{P})\xi_j dR = 0 \tag{27}$$

where $\gamma(\bar{P})$ is the residual function of average pressure. Applying this approach to the average pressure equation (eq. 22), one obtains:

$$\int_R \phi \frac{\partial \bar{P}}{\partial t}\xi_i dR + \int_R \lambda_t \nabla \bar{P}\,\mathbf{k}\nabla\xi_i dR + \int_R (\lambda_w \rho_w + \lambda_n \rho_n)\mathbf{g}\mathbf{k}\nabla\xi_i dR + \frac{1}{2}\int_R (\lambda_w - \lambda_n)\mathbf{k}\nabla p_c \nabla\xi_i dR - \int_R m_t \xi_i dR - \int_{\Gamma_N} (F_i \cdot \mathbf{n})\xi_i d\Gamma_N = 0 \tag{28}$$

where F_i is a flux vector at node i, perpendicular to the boundary Γ_N. The complete set of algebraic differential equations can be obtained by integrating values throughout the nodes in the mesh

$$\sum_{j}^{N}[C_{ij}]\frac{\partial \bar{P}}{\partial t} + \sum_{j}^{N}[K_{ij}]\bar{P}_j = [G_i] + [T_i] + [M_i] + [F_i] \quad i, j = 1,2,\ldots,N \tag{29}$$

where

$$[\mathrm{C_{ij}}] = \int_R \phi \xi_i \xi_j \, dR \tag{30}$$

$$[\mathrm{K_{ij}}] = \int_R \lambda_t \nabla \xi_i \mathbf{k} \nabla \xi_j \, dR \tag{31}$$

$$[\mathrm{G_i}] = -\int_R (\lambda_w \rho_w + \lambda_n \rho_n) \mathbf{g} \mathbf{k} \nabla \xi_i \, dR \tag{32}$$

$$[\mathrm{T_i}] = -\frac{1}{2} \int_R (\lambda_w - \lambda_n) \mathbf{k} \nabla p_c \nabla \xi_i \, dR \tag{33}$$

$$[\mathrm{M_i}] = \int_R m_i \xi_i \, dR \tag{34}$$

$$[\mathrm{F_i}] = \int_{\Gamma_N} (F \cdot \mathbf{n}) \xi_i d\Gamma_N \tag{35}$$

After applying an implicit time-stepping scheme, equation 30 can be reformulated as

$$\sum_j^N \left(\left[C_{ij}^{k+1} \right] + \Delta t \left[K_{ij}^{k+1} \right] \right) \bar{P}_j^{k+1} = \sum_j^N \left[C_{ij}^{k+1} \right] \bar{P}_j^k + \Delta t \left(\left[G_i^k \right] + \left[T_i^k \right] + \left[M_i^k \right] + \left[F_i^k \right] \right) \tag{36}$$

where the Δt is the size of time step and the superscript, k, denotes the present or current time step.

The saturation equation (eq. 25) is solved using the finite volume method. A finite volume sub-grid is constructed by connecting the centroids of the finite element triangles with the midpoints of the neighboring edges (fig. 16). The finite element-wise fluid velocity calculated from the pressure equation (eq. 36) is used in solving the saturation equation. The finite volume formulation including the capillary and buoyancy effects can be written as

$$\int_{v_i} \phi \frac{\partial S_b}{\partial t} dV_i = -\int_{v_i} \nabla \cdot (f_n \mathbf{V_t}) + \int_{v_i} \nabla \cdot (\bar{\lambda} \mathbf{k} \nabla p_c) \, dV_i - \int_{v_i} \nabla \cdot (\bar{\lambda} \mathbf{k} (\rho_w - \rho_n) \mathbf{g}) dV_i + \int_{v_i} m_n dV_i \tag{37}$$

where V_i represents the finite volume of node i.

The volumetric change within a finite volume is equal to the sum of fluxes in and out through each boundary segment. We finally obtain the following numerical form of the fluid-saturation equation after applying Gauss's divergence theorem and imposing an explicit time-marching scheme:

$$S_n^{k+1} = S_n^k + \frac{\Delta t}{\phi A_i}\left(-\sum_j^{N_{si}}(f_{nj}\mathbf{v}_{tj})\cdot\mathbf{n}_j + \sum_j^{N_{si}}(\bar{\lambda}\mathbf{k}\nabla p_c)\cdot\mathbf{n}_j\right) + \frac{\Delta t}{\phi A_i}\left(-\sum_j^{N_{si}}(\bar{\lambda}\mathbf{k}(\rho_w - \rho_n)\mathbf{g})\cdot\mathbf{n}_j + \sum_j^{N_{si}}\frac{1}{3}m_{ne}A_e\right) \quad (38)$$

where N_{si} is the number of neighboring segments of V_i; A_i is the area of the control volume; A_e is the area of the finite element triangle; $\boldsymbol{n}_j$ is the outward normal vector to j^{th} segment, scaled by the length of the segment; N_{ei} is the number of associated finite element triangles, whose fraction is included in V_i. Note that the source/sink term is multiplied by 1/3 because each finite element contributes 1/3 of its volume to the associated finite volume.

Fluid Equations of State

Petroleum includes various gaseous components, and the density of petroleum is strongly dependent on the solubility of lightweight gases in the liquid phase (England and others, 1987; England and Fleet, 1991). With increasing pressure, the solubility of gas increases and the weight of petroleum per unit volume decreases. As a result, the density drops with increasing pressure although it changes a relatively small amount with temperature variance in the same pressure. We used empirical equations of state suggested by Glasø (1980) to obtain the petroleum density in high pressure and temperature conditions, and then the calculated density was fitted to a linear polynomial function for faster computation when applied to the simulation.

$$\rho_{petroleum}(T,P) = a_1 + a_2 T + a_3 P \quad (39)$$

where T is temperature (°C), P is pressure (MPa), and a_1 through a_3 are fitting parameters ($a_1 = 654.01$, $a_2 = 6.48 \times 10^{-2}$, and $a_3 = -3.11$).

The viscosity of liquid petroleum decreases with increasing depth, mostly because of temperature increase. Experimental results under various *P-T* conditions indicate that the dynamic viscosity varies from 5×10^{-4} to 5×10^{-2} Pa·s (England and others, 1987), as compared to water over 20 °C to 130 °C (1.002×10^{-3} to 1.811×10^{-4} Pa·s) (Kestin and others, 1978). We assume that the petroleum viscosity is mostly dependent on temperature,

$$\mu_{petroleum} = b_1(b_2)^T(b_3)^P \quad (40)$$

where T is temperature (°C), P is pressure (MPa), and b_1 through b_3 are empirical fitting parameters ($b_1 = 6.03 \times 10^{-2}$, $b_2 = 0.99$, and $B_3 = 6.98 \times 10^{-7}$).

Model II Setup

A numerical grid for the petroleum migration model is based on the same cross section used in the basin compaction model, covering the southwestern and the central blocks and a series of extensional normal fault zones (fig. 17). A Delaunay triangulation is adopted for generating the mesh in order to reproduce more accurate geology and reduce the grid orientation effect caused by the finite volume method. The finite volume grid is constructed based on the finite element grid by connecting centroids of triangles and the centers of each side. An example of FVM grid construction using triangular finite elements is illustrated in figure 18.

Geohydrologic results (for example overpressure, temperature, and petroleum distribution) obtained from the compaction model are used to set up the initial and boundary conditions for the petroleum migration model. The upper boundary that

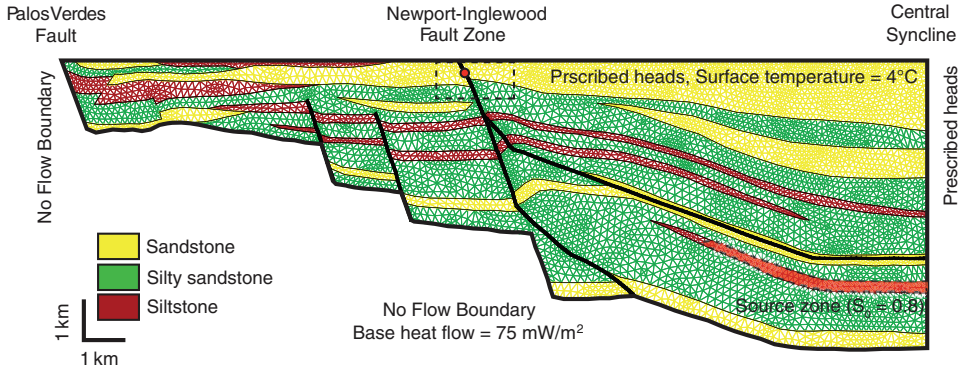

Fig. 17. A numerical grid (12,532 triangular elements) and boundary conditions used in the petroleum migration model.

represents the sea floor is assigned a prescribed-head boundary because our model simulates the petroleum movement in the Pliocene, before subaerial basin uplift by transpressional deformation. The left and bottom sides are set as no-flow-boundary conditions because they are in contact with the low permeability crystalline basement rocks (Norris and Webb, 1990; Redin, 1991). The permeability of those crystalline rocks, in general, range 0.1–0.001 md ($10^{-16} - 10^{-18}$ m^2) in a regional scale and 100 to 1,000 times smaller in a laboratory scale (Brace 1984; Clauser, 1992). For heat flow, a

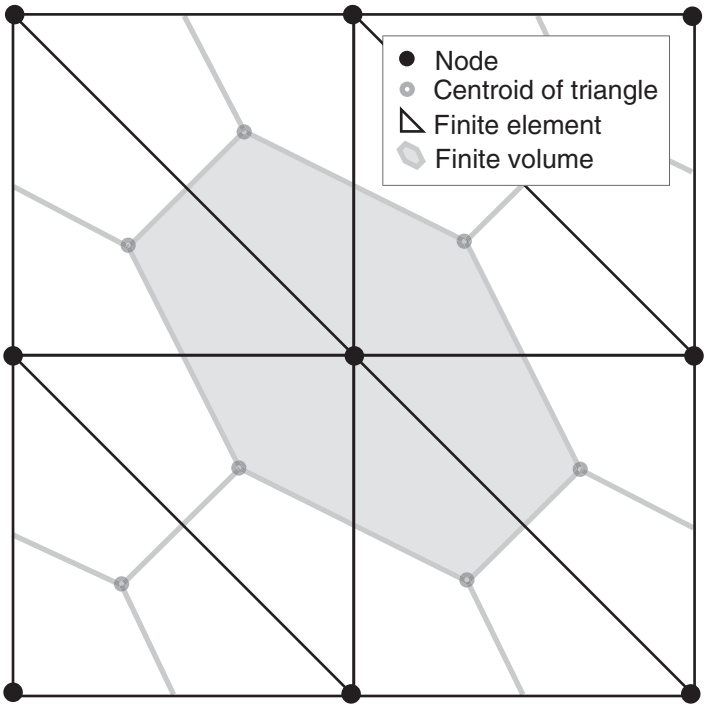

Fig. 18. An example of a finite volume sub-grid extracted from a finite element grid.

uniform heat flux of 70 mW/m^2 is applied to the basement and the seafloor temperature is assigned as $T = 4$ °C, in order to replicate the late Pliocene temperature profile from the compaction model. The heat flow mimics present-day observations ($J \sim 73\ mW/m^2$) based on data from a 3.2 km deep geothermal well in the Los Angeles basin (Sass and others, 1971). Formation water salinity was set 25,000 ppm TDS for the entire domain.

The right boundary is assigned as prescribed pressures whose values are adjusted to reproduce pore pressure conditions in the Pliocene, which was in the compaction-driven flow dominant environment. The initial time step size for the saturation equation is $\Delta t = 5$ years, and the step size is reduced if the results do not satisfy the Courant-Freidrichs-Levy (CFL) condition. The fluid pressure is updated every 100 years.

For the IMPES scheme, the size of the time step, Δt, is limited depending on the element size and the saturation front velocity. If the Δt is too large, the information extends over the next node instead of within on element. This leads to the CFL criterion that determines the maximum step size (Helmig, 1997)

$$Cr = \frac{|\mathbf{v}^{\max}|\Delta t}{\Delta x} < 1 \tag{41}$$

where Cr is the Courant number; $\mathbf{v}^{\max}$ is the maximum velocity within the element. High capillary pressure, in general, is well known for causing stability problems, which usually needs smaller time step sizes. The CFL condition for a 2-D problem is

$$\Delta t\left(\frac{u_x}{\Delta x} + \frac{u_z}{\Delta z}\right) < 1 \tag{42}$$

where u_x and u_z are the velocity components of the constant saturation line in the x-y plane. The stability conditions are generally dependent on both porous media and fluid properties and the size of numerical grid. Major factors restricting time step size are small grid sized, large permeability, and large gradients in capillary pressure (Dekker and Abriola, 2000).

The pore space is initially fully saturated by groundwater except a petroleum source zone. The initial petroleum saturation is inferred from the results of the compaction model. From figure 15C, only the area having high potential for petroleum production (greater than 40 mg per g of source rock) is assumed to be the petroleum source zone. Initially the source zone is nearly saturated with petroleum ($S_n \sim 0.8$), considering the irreducible water saturation is set to 0.2 for siltstone.

Although the timing for the start of the massive hydrocarbon migration is not certain, we assume that accumulated petroleum started to migrate during the late Pliocene-Pleistocene deformation, considering the tectonic history and the modeled petroleum volume generated in the basin. Wright (1991) indicated many petroleum reservoirs associated with geologic structures were formed by the reactivation of faults by the late Pliocene deformation. This deformation also triggered deep thrust faulting by compressional tectonic forces (Shaw and Suppe, 1996), which can provide sufficient dynamic channels for petroleum migration. The modeling results also indicate the total volume of petroleum is sufficiently accumulated during the Pliocene (fig. 16). The generated petroleum is expelled from the pores in the source rock by fluid volume expansion accompanied by kerogen conversion. The fluid fluxes in the basin also show the highest values during this period (fig. 13). Based on the observations listed above, it would be reasonable to presume that the petroleum migration began in middle to late Pliocene, and subsequent phases of tectonic deformation may have accelerated this process.

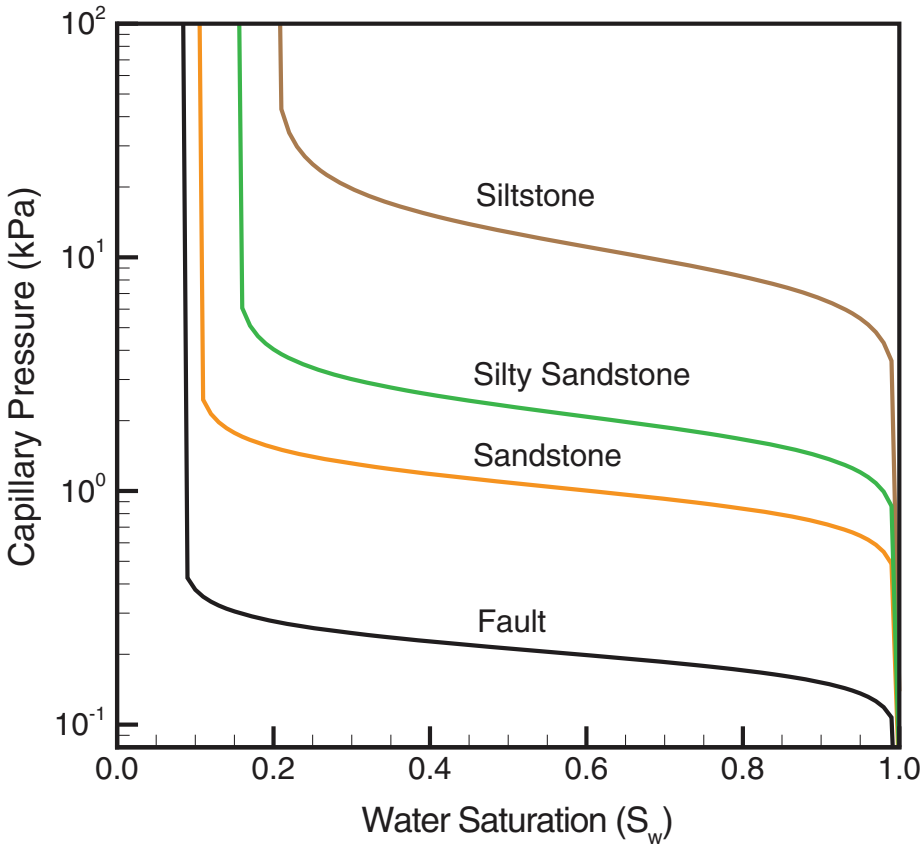

Fig. 19. Log-linear plots of capillary pressure versus fluid saturation, calculated using the van Genuchten equation.

The van Genuchten equations (van Genuchten, 1980) are used for calculation of the nonlinear relationship between saturation, capillary pressure and relative permeability. For most cases, capillary pressure increases as the pore water drains and the lithology of the porous medium affects the shape of the characteristic curve. In general, coarser-grained material shows a steeper increase in the capillary pressure with the decrease of water saturation. Capillarity model parameters were chosen in the range of typical sandstone and siltstone obtained from other publications (Levorsen, 1967; Wendebourg, ms, 1994; Bloomfield and others, 2001).

The characteristic capillary pressure curves for sedimentary formations used in the model are plotted in figure 19. The capillary pressure of the siltstone is considered higher than other rock types due to its higher contents of clay and other fine-grained materials. It also has the lowest permeability value compared to other sediment layers.

Relative permeabilities of the water and petroleum phases (k_{rw}, k_{rn}) are also functions of effective saturation. We assume

$$k_{rw} = S_e^{\varepsilon}\left(1 - \left(1 - S_e^{\frac{1}{m}}\right)^m\right)^2 \tag{43}$$

$$k_{rn} = (1 - S_e)^{\gamma}\left(1 - S^{\frac{1}{m}}\right)^{2m} \tag{44}$$

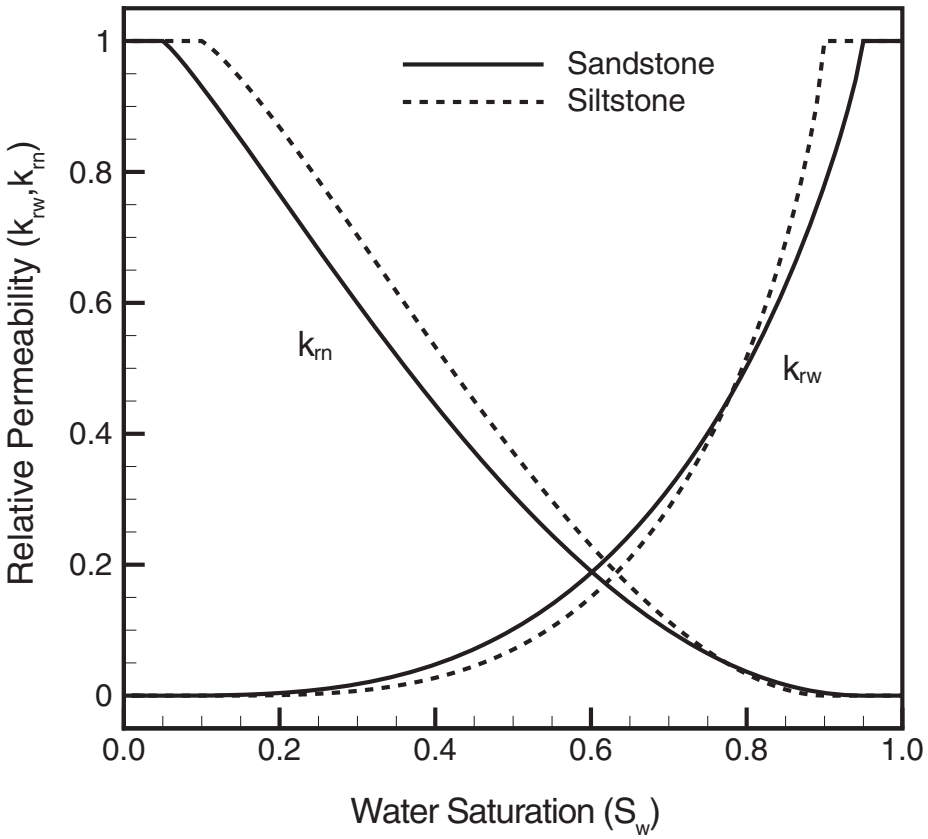

Fig. 20. Relative permeability changes of sandstone and siltstone with respect to water saturation, calculated using the van Genuchten equations (eqs. 42 and 43).

where S_e is the effective saturation ($S_e = (S_w\text{-}S_{wr})/(1\text{-}S_{wr})$), and S_{wr} is the irreducible water saturation. The constants m and n are called van Genuchten parameters ($m = 1–1/n$), which reflect the lithologic character of the porous medium. The coefficients ε and γ are pore connectivity form parameters, which are usually 1/2 and 1/3, respectively (Helmig, 1997).

Relative permeability curves used for the model are plotted in figure 20. The relative permeability of each phase increases, in general, with its saturation. Functions of relative permeability are often considered complementary functions that sum to unity. As a result, if the petroleum phase occupies some portion in the sedimentary rock with high saturation, groundwater will flow around the area rather than penetrate because of the low relative permeability with respect to the water phase.

Fault zones are simulated as fluid flow conduits in this model, so the intrinsic permeability of the fault zone (**k**) is assigned to 5 ~ 50 md, which is closely matched with that of the compaction model. Low entry pressure for the fault zone is assumed because field observations often report that large-scale faults are usually brecciated and filled with relatively permeable material. Faults in the Los Angeles basin also includes many open fractures, which can be considered typical characteristic features of dilatant normal faults (Aydin, 2000). Other important hydrogeologic parameters for the simulation are listed in table 5.

TABLE 5

Hydrogeologic properties for petroleum migration model

Hydrogeologic unit	Intrinsic permeability k_x (m^2)	Anisotropy Ratio (k_x/k_z)	Porosity φ	Thermal conductivity λ (W/m°C)	Capillary parameters (van Genuchten model)	
					n	A (Pa-1)
Sandstone	4.0×10^{-14}	10.0	0.20	3.0	6.0	2.5×10^{-3}
Silty sandstone	2.0×10^{-14}	100.0	0.15	2.8	4.0	4.0×10^{-4}
Siltstone	5.0×10^{-15}	100.0	0.10	2.5	3.0	5.0×10^{-5}
Fault	1.0×10^{-14}	1.0	0.15	3.0	6.0	1.0×10^{-3}

Model II Results

Figure 21 illustrates the computed petroleum saturation for three time stages showing migration patterns and pathways from source rocks to oil reservoirs in the NIFZ. The simulation time t = 0 corresponds to the end of Pliocene. For the first 60 kyr, the petroleum in the source area is dispersed and elongated along the fault plane, but also rises and saturates an overlying formation by buoyancy (fig. 21B). By 120 kyr, a few preferential migration routes to oil reservoirs are established, and petroleum plumes arrive at the top of the NIFZ. Petroleum promptly flows through both a fault structure and a permeable sandstone layer that links to the middle part of the NIFZ (fig. 21C). The next two figures capture the further developments of the migration pattern (figs. 21D and 21E). The reservoir pooling area in the NIFZ gradually expands due to continuous transport from the source beds, while saturation of the source zone is simultaneously decreased. The petroleum in the basin center also moves toward the fault zone, driven by buoyancy- and compaction-driven groundwater flow and being effectively guided by less permeable siltstone layers. The magnitude of compaction-driven flow during the simulation is basically controlled by the imposed head values on the right boundary. According to the results of this simulation, the continuity of siltstone layers is very important for petroleum accumulation. The low permeability and high oil-entry pressure of the siltstones allow oil to accumulate under the formation, thereby creating strong focused flow to the reservoir site while preventing dispersion by buoyant flow.

Petroleum and groundwater flux distributions are illustrated in figure 22. Water velocities (fig. 22A) are generally high at the basin center at a depth range of 3 to 4 km where overpressure by the sediment compaction is the strongest. The highest velocity is found in the upper NIFZ, but the rest of the fault zone and sandstone layers also have relatively high water velocities. The petroleum velocity distribution (fig. 22B) is very similar to that of petroleum saturation because the relative permeability of a petroleum phase has a large value at a high saturation zone. Petroleum velocities are especially high at the NIFZ and the central thrust fault attached to it. The maximum values for water and petroleum velocities obtained from the simulation are 0.61 m/yr and 0.19 m/yr, respectively.

Temporal variations of petroleum saturations at the NIFZ (the exact location is marked as a red circle in fig. 17) are plotted in figure 23A, which shows the effect of the fault permeability on migration speed and saturation fluctuation. For the intrinsic permeability of the fault, k = 20 md (2.0×10^{-14} m^2), the total migration time from the source zone to the top of the NIFZ takes ~130 kyr. The migration time increases to about 160 kyr when the fault k drops to 10 md. The sharp increase of the petroleum saturation in the fault zone probably indicates fast fluid flow and low dispersion due to high permeability and low capillary pressure assigned to the fault. In both cases, saturations remain within the range of 0.3 to 0.4.

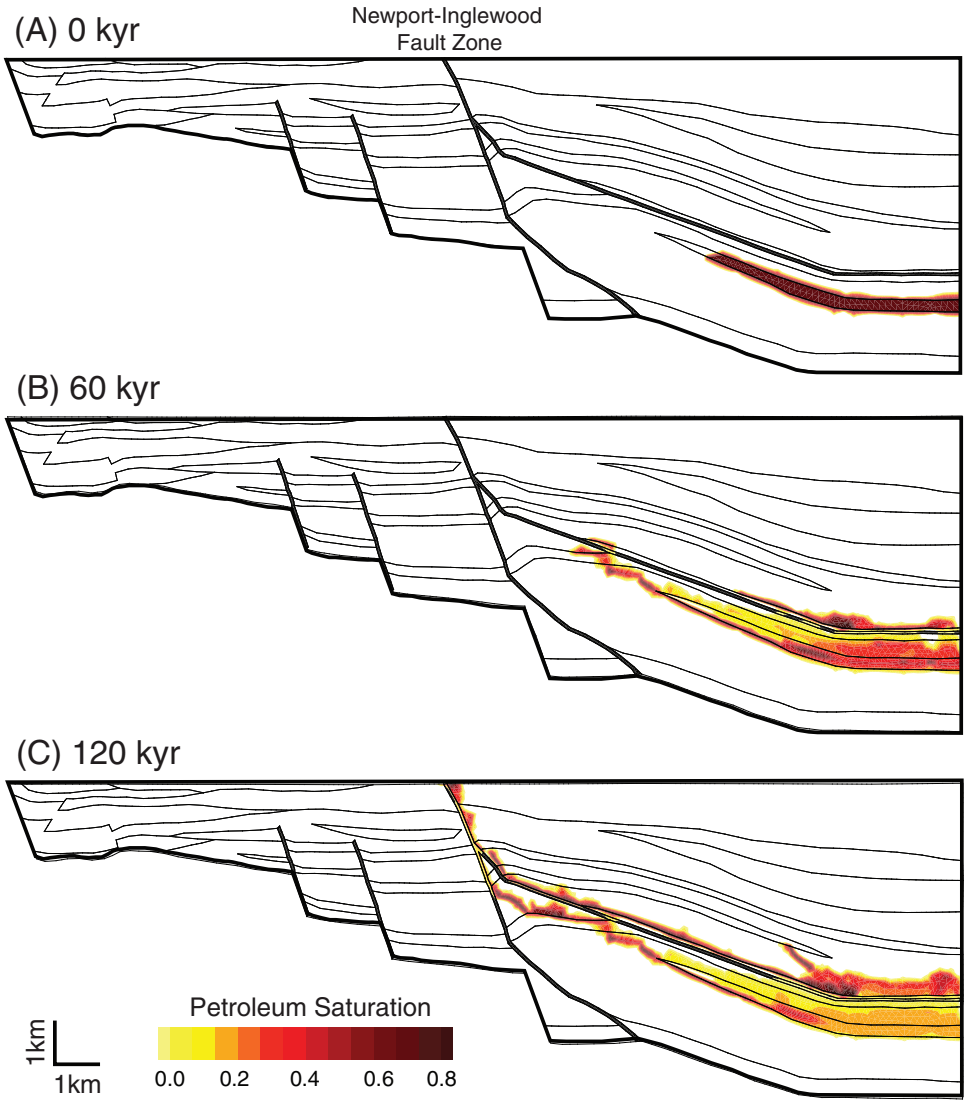

Fig. 21. Simulated petroleum saturations showing effects of NIFZ on petroleum migration in the LA basin. (A) 0 yr, (B) 60 kyr, (C) 120 kyr, (D) 180 kyr, and (E) 240 kyr.

Hayba and Bethke (1995) also calculated the petroleum migration travel time from the central basin to the West Coyote oil field located in the eastern part of the Los Angeles basin (total distance is about 13 km). From these calculations, they estimated the total travel time to be about 60 to 120 kyr depending on the sediment compaction history. Those numbers are generally comparable to our results, although the direct comparison is difficult due to different modeling approaches.

Figures 23B and 23C show how the pore water and petroleum velocity change at the fault zone during the simulation time. The petroleum velocity shows abrupt increase immediately after the fault zone is saturated at ~120 kyr. The magnitude of petroleum velocity is about 8 mm/yr when the fault $k = 20$ md, and it is approximately

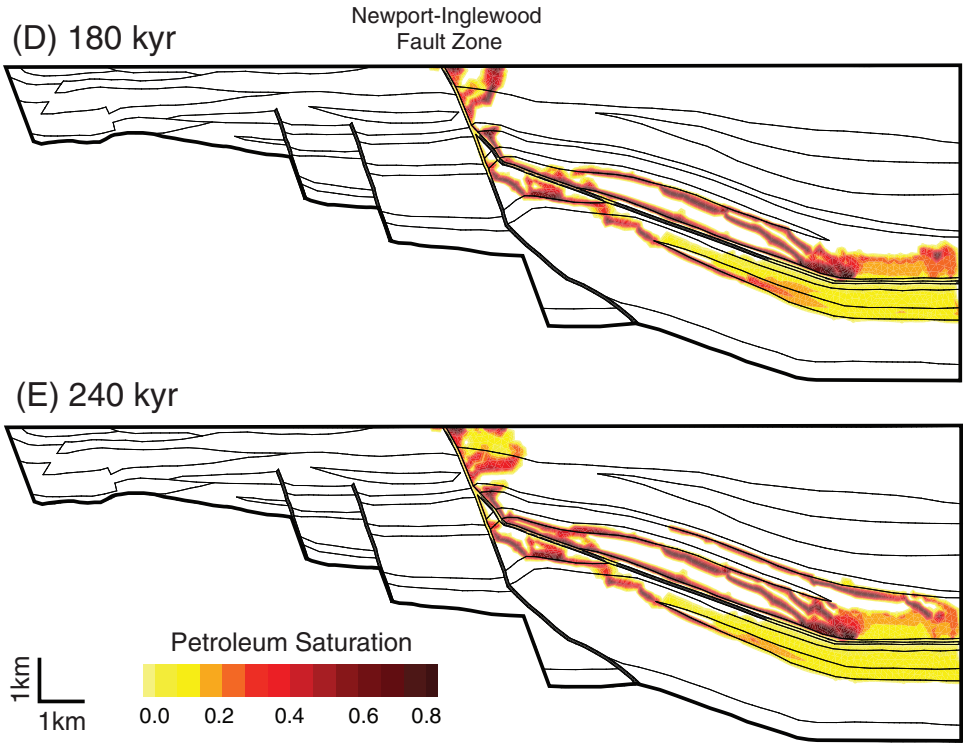

Fig. 21. (continued).

two times larger than the velocity obtained from the simulation with the fault $k = 10$ md. It is also notable that the petroleum velocity with higher fault permeability shows more fluctuation in magnitude. In contrast, water velocity decreases after the petroleum is introduced in the fault zone because the relative permeability of water drops accordingly. In the case of fault $k = 20$ md, water velocity sharply drops from 0.3 to 0.2 m/yr and decreases slowly to about 180 mm/yr. The magnitude change in velocity becomes smaller in the case of fault $k = 10$ md and the fluctuation after the velocity drop is also minor.

DISCUSSION

Sensitivity tests on critical parameters including the fault permeability and the compaction-driven flow intensity are implemented to understand their roles on total petroleum volume trapped in oil reservoirs associated with NIFZ. We first compared temporal variations of total petroleum volume computed from different fault permeability settings. The permeability is changed within the range of 5 to 50 md and the values are considered fair to good conductivity conditions based on the oil reservoir classification done by Levorsen (1967).

The total petroleum volume in the NIFZ is computed by integrating oil volume entering into a 2 km by 1 km area containing the NIFZ and its vicinity (the dashed lines drawn in fig. 17). We assumed a characteristic length of 10 km to obtain the 3-D volume value from the 2-D model. The assumed value is a rough approximation of the total length of the saturated oil field along the NIFZ.

In general, the total petroleum volume accumulated increased with time and reached a steady state after a certain period (fig. 24A). The fault permeability

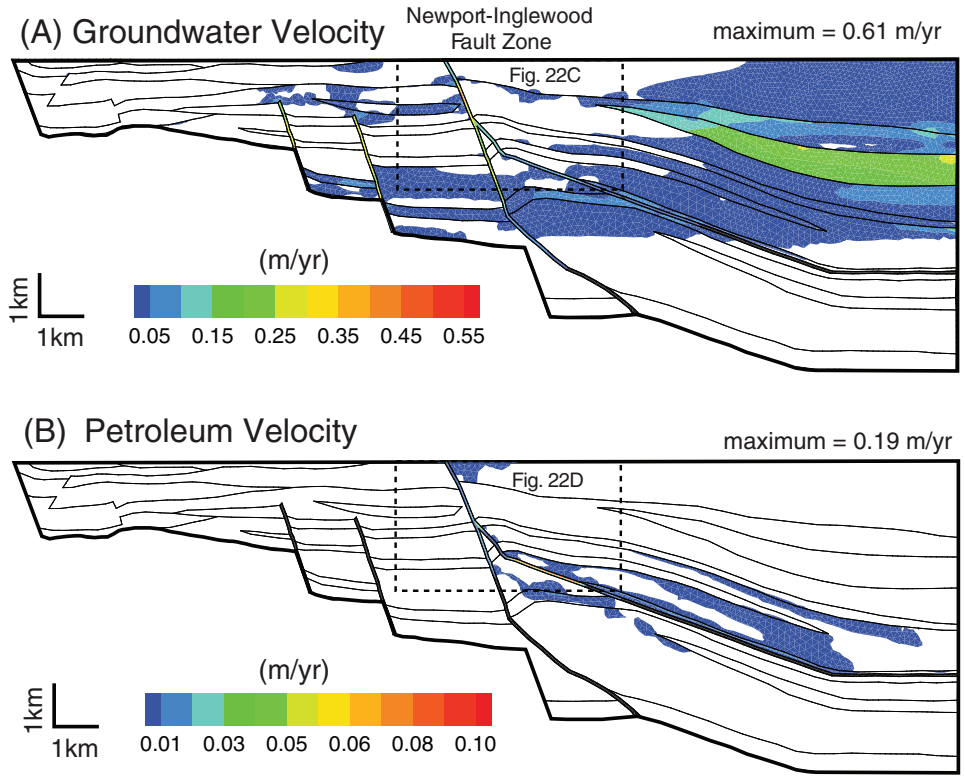

Fig. 22. Petroleum and groundwater velocity distributions during the migration process (t = 240 kyr). Figures inside of the dashed boxes are zoomed in figs. 22C and 22D.

influences the timing of accumulation in the reservoir; therefore, the higher permeability a model has, the shorter travel time from the source to the reservoir. For example, a high permeability case, for example k = 50 md, takes about 90 kyr to migrate petroleum to first arrive in the reservoir area (a breakthrough time); whereas the low permeability model, for example k = 5 md takes more than 220 kyr. The fault zone permeability also influences the rate of accumulation, so the slope of total volume is steeper in high permeability models and becomes lower with the permeability decrease.

The elapsed time needed to accumulate the total amount of petroleum in the NIFZ can also be inferred from the modeling results. The horizontal line in figure 24A represents the value of 2 Gbbl (3.16×10^8 m^3), which is the estimated total petroleum volume reserved in the major oil reservoirs located along the NIFZ. When k = 50 md, the total time needed to reach the current amount of oil volume is about 120 kyr, and the time increases to about 180 kyr when k = 20 md. For a low permeability case with k = 10 md, it takes over 300 kyr to form oil reservoirs in the NIFZ having the present amount of reserved petroleum.

The intensity of overpressure caused by sediment compaction is also an important factor to consider when determining the quantitative aspects of the petroleum migration, so we did a similar sensitivity study to characterize the effects of the compaction-driven flow on the speed and volume of the migration. Temporal variations of total petroleum volume under both high and low subsurface pressure

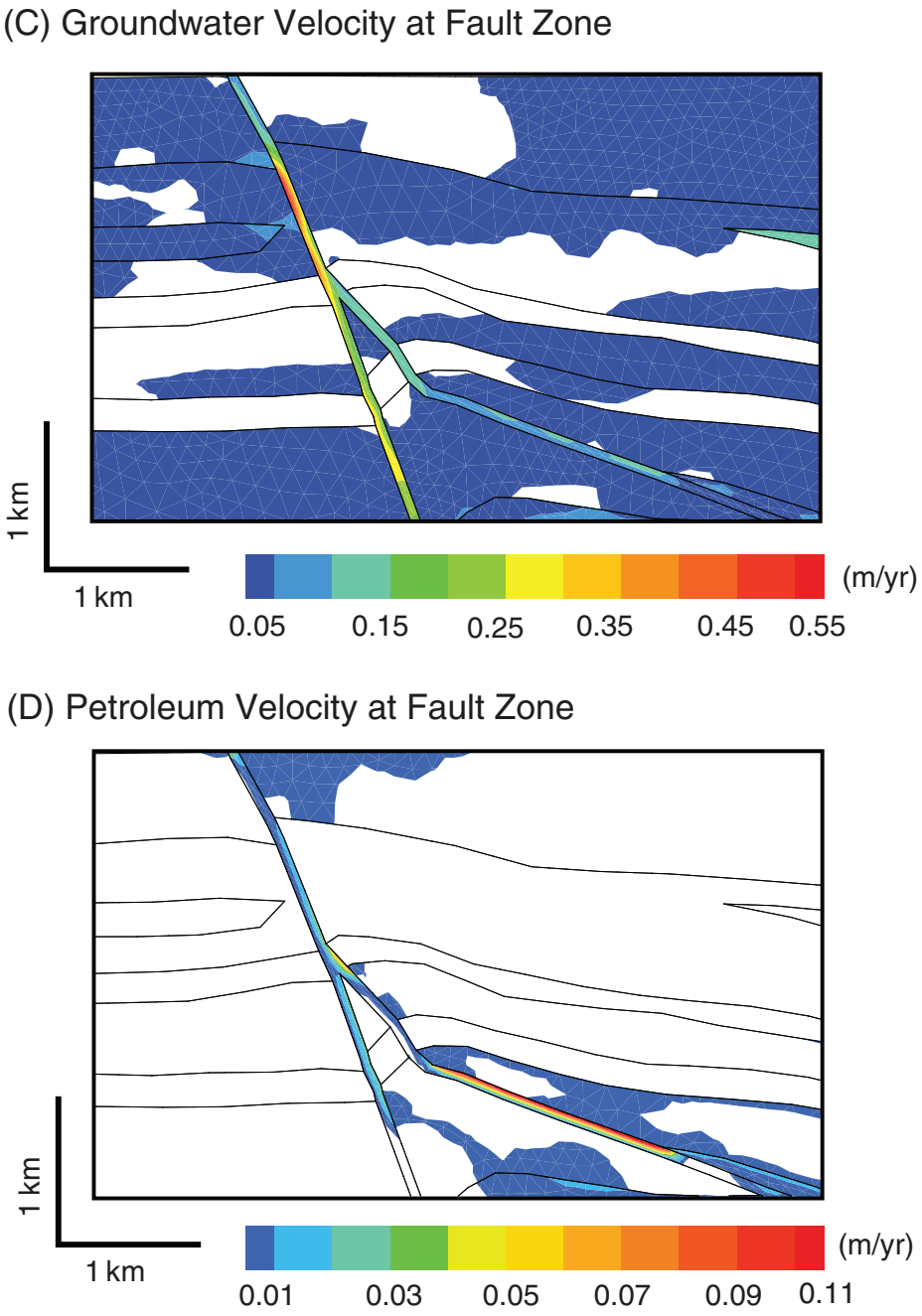

Fig. 22. (continued).

conditions are plotted in figure 24B. We controlled the overpressure intensity in the model by modifying the value of pressure boundary conditions. Pressure differences between the basin center and the top surface are 200 m for the high groundwater flow

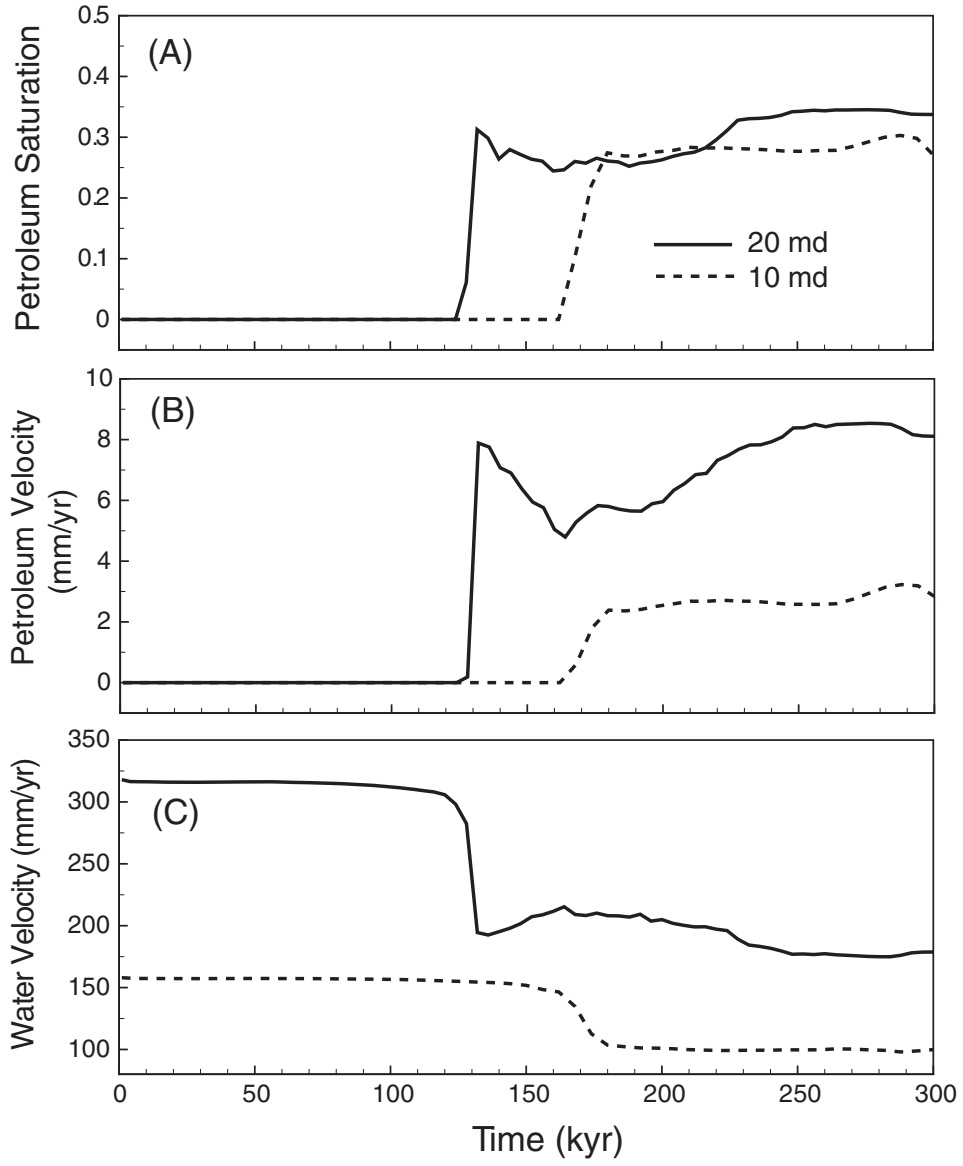

Fig. 23. Temporal variations of multiphase fluid properties at the fault zone (marked as a circle in fig. 17).

case and 100 m for the low flow case. For both cases, the fault permeability is maintained as the same value of 30 md.

The intensity of sediment compaction influences migration speed and therefore accumulation rate. In the high compaction-driven flow case (Δh = 200 m), petroleum first arrives at the reservoir after about 110 kyr while the low flow case (Δh = 100 m) takes about 220 kyr. The accumulation rate that can be inferred from the slope of the curve is also high in the high flow case. The low-flow case takes about 300 kyr to recharge the reservoirs in the NIFZ with the current level (~2 Gbbl), which is twice as long as that of the high-flow model.

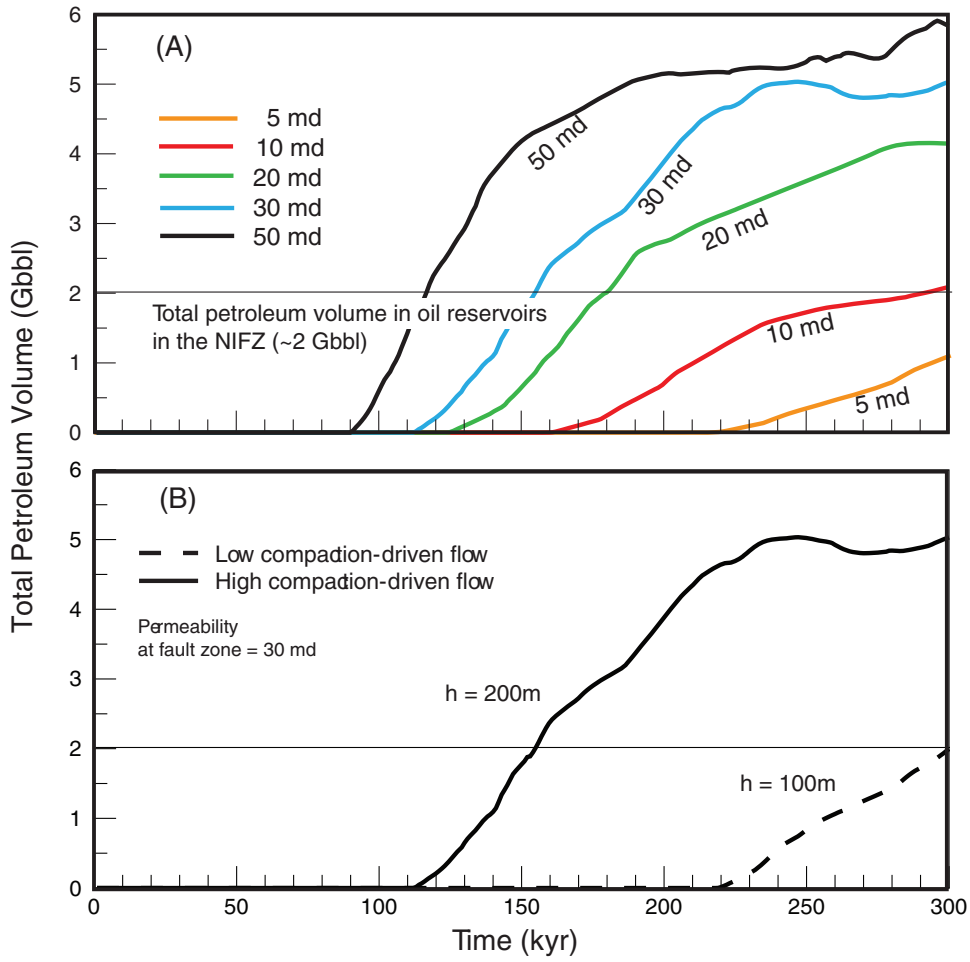

Fig. 24. Effects of hydrogeologic factors on total petroleum volume accumulated in the NIFZ: (A) fault permeability, (B) compaction-driven flow intensity.

The relationship among petroleum travel time from the source to the reservoir, fault permeability, and compaction-driven flow intensity is plotted in figure 25. The travel time exponentially increases with decreasing permeability. The basinal groundwater flow intensity also affects the total petroleum travel time, and low compaction-driven flow generally retards the migration process. Also notable is that the reduction in the groundwater flow causes the range of overall travel time to increase, suggesting the role of the large-scale fault zone in petroleum migration may become more significant if the compaction-driven flow is weak and other driving forces for migration are not available.

CONCLUSIONS

Based on this multiphase flow study, we have concluded the following:

1. The magnitude of compaction-driven flow and the temperature distribution in the LA basin were controlled mainly by tectonic history. The timing and intensity of the tectonic subsidence are closely related to the temporal varia-

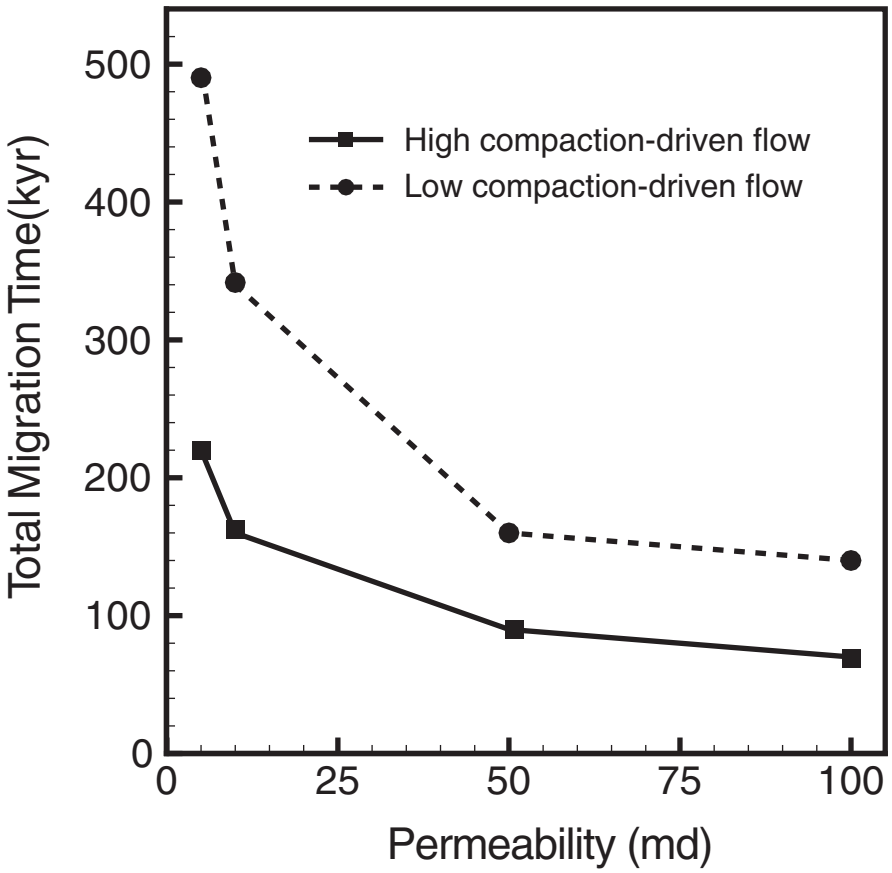

Fig. 25. Effects of fault permeability and fluid overpressure intensity on total petroleum migration time based on the modeling results.

tions of groundwater flow and temperature, and the possible source generation area. The timing of petroleum generation is also synchronized with the tectonic events. In addition, the total petroleum volume generated is high when the basinal extension activity occurs.

2. The petroleum migration model suggests that large-scale fault zones and juxtaposed aquifer networks act as preferential pathways for petroleum flow, which enable faster and more focused or channeled migration to shallow reservoirs. The total migration time from the source zone to first arrive in the NIFZ is about 120 kyr when the fault $k = 20$ md, and it takes about 180 kyr to fill the reservoirs to the current level of total oil volume. Possible driving forces for the migration are hydrodynamic pressure created by sediment compaction and buoyancy.
3. Sensitivity tests on fault permeability suggest that total migration time from the source to first arrive in the NIFZ can vary the range of 90 to 220 kyr, depending on values of fault k varying from 50 md to 5 md. Total time required for accumulating the current amount of petroleum in the NIFZ is about 120 kyr if the fault $k = 50$ md, and may extended to over 300 kyr if fault k becomes less than 10 md. Decrease in the compaction-driven flow also retards the petroleum migration speed and accumulation.

ACKNOWLEDGMENT

We would like to thank the U.S. Department of Energy – Basic Energy Sciences for funding this research (Grant number: DE-FG02-96ER14620), and the GDL Foundation for a scholarship awarded to the first author. We also appreciate AJS reviewers for very constructive comments and discussion.

Appendix

Symbol Notation

Symbol	Meaning
c_f	specific heat capacity of groundwater/ pore water
c_s	specific heat capacity of sediment
H	hydraulic head
$\boldsymbol{K}$	intrinsic permeability
P	fluid pressure
p_c	capillary pressure
q	Darcy flux
T	temperature
R_t	kerogen transformation ratio
Z	elevation above arbitrary datum
α_L	longitudinal dispersivity
α_T	transverse dispersivity
β_v	vertical bulk compressibility coefficient
Γ	additional fluid sources/sinks per unit volume
ϕ	porosity
ϕ_0	initial porosity (at the land surface)
ϕ_{ir}	irreducible porosity
λ	thermal dispersivity
Λ	thermal expansion coefficient
μ_f	viscosity of groundwater
μ_r	relative viscosity
ρ_{oil}	density of oil (petroleum liquid)
ρ_k	density of kerogen
ρ_r	relative density
ρ_f	density of groundwater
ρ_s	density of sediment
σ_e	effective stress
σ_v	total vertical stress

References

Athy, L. F., 1930, Density, porosity and compaction of sedimentary rocks: AAPG Bulletin, n. 14, n. 1, p. 1–24.

Aydin, A., 2000, Fractures, faults, and hydrocarbon entrapment, migration and flow: Marine and Petroleum Geology, v. 17, n. 7, p. 797–814, http://dx.doi.org/10.1016/S0264-8172(00)00020-9

Aziz, K., and Settari, A., 1979, Petroleum Reservoir Simulation: London, Applied Science Publisher, 476 p.

Bear, J., 1972, Dynamics of Fluids in Porous Media: New York, Elsevier, 764 p.

Bethke, C. B., and Corbet, T. F., 1988, Linear and nonlinear solutions for one-dimensional compaction flow in sedimentary basins: Water Resources Research, v. 24, n. 3, p. 461–467, http://dx.doi.org/10.1029/WR024i003p00461

Bethke, C. M., 1985, A numerical model of compaction-driven groundwater flow and heat transfer and its application to the paleohydrology of intracratonic sedimentary basins: Journal of Geophysical Research-Solid Earth, v. 90, n. B8, p. 6817–6828, http://dx.doi.org/10.1029/JB090iB08p06817

Bethke, C. M., Reed, J. D., and Oltz, D. F., 1991, Long-range petroleum migration in the Illinois Basin: American Association of Petroleum Geologists Bulletin, v. 75, n. 5, p. 925–945.

Biddle, K. T., 1991, The Los Angeles basin: an overview, *in* Biddle, K. T., editor, Active Margin Basins: AAPG Memoir, v. 52, p. 1–24.

Bilodeau, W. L., Bilodeau, S. W., Gath, E. M., Oborne, M., and Proctor, R. J., 2007, Geology of Los Angeles, California, United States of America: Environmental & Engineering Geoscience, v. 13, n. 2, p. 99–160, http://dx.doi.org/10.2113/gseegeosci.13.2.99

Blake, G. H., 1991, Review of the Neogene biostratigraphy and stratigraphy of the Los Angeles Basin and implications for basin evolution, *in* Biddle, K. T., editor, Active Margin Basins: AAPG Memoir, v. 52, p. 135–184.

Bloomfield, J. P., Gooddy, D. C., Bright, M. I., and Williams, P. J., 2001, Pore-throat size distributions in Permo-Triassic sandstones from the United Kingdom and some implications for contaminant hydrogeology: Hydrogeology Journal, v. 9, n. 3, p. 219–230, http://dx.doi.org/10.1007/s100400100135

Boles, J. R., and Ramseyer, K., 1987, Diagenetic carbonate in Miocene sandstone reservoir, San Joaquin basin, California: American Association of Petroleum Geologists Bulletin, v. 71, n. 12, p. 1475–1487.

Boles, J. R., Eichhubl, P., Garven, G., and Chen, J., 2004, Evolution of a hydrocarbon migration pathway along basin-bounding faults: Evidence from fault cement: American Association of Petroleum Geologists Bulletin, v. 88, n. 7, p. 947–970, http://dx.doi.org/10.1306/02090403040

Bostick, N. H., Cashmann, S. M., McCulloh, T. H., and Waddle, C. T., 1978, Gradients of vitrinite reflectance and present temperature in the Los Angeles and Ventura Basins, California, *in* Oltz, D. F., editor, Symposium in Geochemistry: Low Temperature Metamorphism of Kerogen and Clay Minerals: Pacific Section, SEPM, p. 65–96.

Brace, W. F., 1984, Permeability of crystalline rocks; new *in situ* measurements: Journal of Geophysical Research-Solid Earth, v. 89, n. B6, p. 4327–4330, http://dx.doi.org/10.1029/JB089iB06p04327

California Department of Conservation, 1992, California Oil and Gas Fields: Volume II - Southern, Central Coastal, and Offshore California Oil and Gas Fields: California Department of Conservation, Division of Oil, Gas, and Geothermal Resources, 645 p.

Campbell, R. H., and Yerkes, R. F., 1976, Cenozoic evolution of the Los Angeles basin area - relation to plate tectonics, *in* Howell, D. G., editor, Aspects of the geologic history of the California continental borderland: Pacific Section, AAPG Miscellaneous Publication, v, 24, p. 541–558.

Carruthers, D., 2003, Modeling of secondary petroleum migration using invasion percolation techniques, *in* Duppenbecker, S., and Marzi, R., editors, Multidimensional basin modeling: AAPG/Datapages Discovery Series, v. 7, p. 21–37.

Carruthers, D., and Ringrose, P., 1998, Secondary oil migration: oil-rock contact volumes, flow behaviour and rates, *in* Parnell, J., editor, Dating and Duration of Fluid Flow and Fluid-Rock Interaction: Geological Society, London, Special Publications, v. 144, p. 205–220, http://dx.doi.org/10.1144/GSL.SP.1998.144.01.16

Cavanagh, A., 2013, Benchmark calibration and prediction of the Sleipner CO_2 plume from 2006 to 2012: Energy Procedia, v. 37, p. 3529–3545, http://dx.doi.org/10.1016/j.egypro.2013.06.246

Chen, Z., Huan, G., and Ma, Y., 2006, Computational Methods for Multiphase Flows in Porous Media: Philadelphia, SIAM, 531 p.

Clayton, J. L., and Swetland, P. J., 1980, Petroleum generation and migration in Denver Basin: American Association of Petroleum Geologists Bulletin, v. 64, n. 10, p. 1613–1633.

Clauser, C., 1992, Permeability of crystalline rocks: Eos, Transactions American Geophysical Union, v. 73, n. 21, p. 233–238, http://dx.doi.org/10.1029/91EO00190

Cooke, M. L., and Dair, L. C., 2011, Simulating the recent evolution of the southern big bend of the San Andreas fault, Southern California: Journal of Geophysical Research-Solid Earth, v. 116, B04405, http://dx.doi.org/10.1029/2010JB007835

Corbet, T., and Bethke, C. M., 1992, Disequilibrium fluid pressures and groundwater flow in the Western Canada sedimentary basins: Journal of Geophysical Research, n. 97, n. B5, p. 7203–7217, http://dx.doi.org/10.1029/91JB02993

Creaney, S., and Allan, J., 1990, Hydrocarbon generation and migration in the Western Canada sedimentary basin: Geological Society, London, Special Publications, v. 50, p. 189–202, http://dx.doi.org/10.1144/GSL.SP.1990.050.01.9

Creaney, S, Allan, J., Cole, K. S., Fowler, M. G., Brooks, P. W., Osadetz, K. G., Macqueen, R. W., Snowdon, L. R., and Riediger, C. L., 1994, Petroleum generation and migration in the Western Canada Sedimentary Basin: Geological Atlas of the Western Canada Sedimentary Basin, p. 455–468.

Crouch, J. K., and Suppe, J., 1993, Late Cenozoic tectonic evolution of the Los Angeles Basin and inner California borderland; A model for core complex-like crustal extension: Geological Society of America Bulletin, v. 105, n. 11, p. 1415–1434, http://dx.doi.org/10.1130/0016-7606(1993)1052.3.CO;2

Davis, T. L., Namson, J., and Yerkes, R. F., 1989, A cross section of the Los Angeles Area: Seismically active fold and thrust belt, the 1987 Whittier Narrows earthquake, and earthquake hazard: Journal of Geophysical Research-Solid Earth, v. 94, n. B7, p. 9644–9664, http://dx.doi.org/10.1029/JB094iB07p09644

Dekker, T. J., and Abriola, L. M., 2000, The influence of field-scale heterogeneity on the infiltration and entrapment of dense nonaqueous phase liquids in saturated formations: Journal of Contaminant Hydrology, v. 42, n. 2–4, p. 187–218, http://dx.doi.org/10.1016/S0169-7722(99)00092-3

Demaison, G., and Huizinga, B. J., 1991, Genetic classification of petroleum systems: AAPG Bulletin, n. 75, n. 10, p. 1626–1643.

Domenico, P. A., and Palciauskas, V. V., 1979, Thermal expansion of fluids and fracture initiation in compacting sediments: Geological Society of America Bulletin, v. 90, n. 6, p. 953–979, http://dx.doi.org/10.1130/GSAB-P2-90-953

Dow, W. G., 1974, Application of oil correlation and source rock data to exploration in Williston basin: American Association of Petroleum Geologists Bulletin, v. 58, n. 7, p. 1253–1262.

Durlofsky, L. J., 1993, A triangle based mixed finite element - finite volume technique for modeling two phase flow through porous media: Journal of Computational Physics, v. 105, n. 2, p. 252–266, http://dx.doi.org/10.1006/jcph.1993.1072

_____ 1994, Accuracy of mixed and control volume finite element approximations to Darcy velocity and related quantities: Water Resources Research, v. 30, n. 4, p. 965–973, http://dx.doi.org/10.1029/94WR00061

Eichhubl, P., Davatzes, N. C., and Becker, S. P., 2009, Structural and diagenetic control of fluid migration and cementation along the Moab fault, Utah: AAPG Bulletin, v. 93, n. 5, p. 653–681, http://dx.doi.org/10.1306/02180908080

England, W. A., and Fleet, A. J., 1991, Petroleum Migration: Geological Society, London, Special Publications, v. 59, 280 p.

England, W. A., Mackenzie, A. S., Mann, D. M., and Quigley, T. M., 1987, The movement and entrapment of petroleum fluids in the subsurface: Journal of the Geological Society, London, v. 144, n. 2, p. 327–347, http://dx.doi.org/10.1144/gsjgs.144.2.0327

Fisher, M. A., Langenheim, V. E., Nicholson, C., Ryan, H. F., and Sliter, R. W., 2009, Recent developments in understanding the tectonic evolution of the Southern California offshore area: Implications for earthquake-hazard analysis, *in* Lee, H. J., and Normark, W. R., editors, Earth Science in the Urban Ocean: The Southern California Continental Borderland: GSA Special Papers, v. 454, p. 229–250, http://dx.doi.org/10.1130/2009.2454(4.2)

Forsyth, G. E., and Wasow, W. R., 1960, Finite-Difference Methods for Partial Differential Equations: New York, John Wiley & Sons Inc., Applied Mathematics Series, 444 p.

Fritsche, A. E., 1998, Miocene paleogeography of southwestern California and its implications regarding basin terminology: International Geology Review, v. 40, n. 5, p. 452–470, http://dx.doi.org/10.1080/00206819809465219

Garden, I. R., Guscott, S. C., Burley, S. D., Foxford, K. A., Walsh, J. J., and Marshall, J., 2001, An exhumed palaeo-hydrocarbon migration fairway in a faulted carrier system, Entrada Sandstone of SE Utah, USA: Geofluids, v. 1, n. 3, p. 195–213, http://dx.doi.org/10.1046/j.1468-8123.2001.00018.x

Garven, G., 1989, A hydrogeologic model for the formation of the giant oil sands deposits of the Western Canada Sedimentary Basin: American Journal of Science, v. 289, n. 2, p. 105–166, http://dx.doi.org/10.2475/ajs.289.2.105

Geiger, S., Roberts, S., Matthai, S. K., Zoppou, C., and Burri, A., 2004, Combining finite element and finite volume methods for efficient multiphase flow simulations in highly heterogeneous and structurally complex geologic media: Geofluids, v. 4, n. 4, p. 284–299, http://dx.doi.org/10.1111/j.1468-8123.2004.00093.x

Geiger, S., Driesner, T., Heinrich, C. A., and Matthäi, S. K., 2006a, Multiphase thermohaline convection in the Earth's crust: I. A new finite element - Finite volume solution technique combined with a new equation of state for NaCl-H_2O: Transport in Porous Media, v. 63, n. 3, p. 399–434, http://dx.doi.org/10.1007/s11242-005-0108-z

_____ 2006b, Multiphase thermohaline convection in the Earth's crust: II. Benchmarking and application of a finite element - Finite volume solution technique with a NaCl-H_2O equation of state: Transport in Porous Media, v. 63, n. 3, p. 435–461, http://dx.doi.org/10.1007/s11242-005-0109-y

Geiser, P. A., and Seeber, L., 2008, Three-dimensional seismo-tectonic imaging: An example from the Southern California Transverse Ranges: Journal of Structural Geology, v. 30, n. 7, p. 929–945, http://dx.doi.org/10.1016/j.jsg.2008.02.010

Glasø, Ø., 1980, Generalized pressure-volume-temperature correlations: Journal of Petroleum Technology, v. 32, n. 5, p. 785–795, http://dx.doi.org/10.2118/8016-PA

Griffith, W. A., and Cooke, M. L., 2005, How sensitive are fault-slip rates in the Los Angeles basin to tectonic boundary conditions?: Bulletin of the Seismological Society of America, v. 95, n. 4, p. 1263–1275, http://dx.doi.org/10.1785/0120040079

Harrison, W. J., and Summa, L. L., 1991, Paleohydrology of the Gulf of Mexico Basin: American Journal of Science, v. 291, n. 2, p. 109–176, http://dx.doi.org/10.2475/ajs.291.2.109

Hayba, D. O., and Bethke, C. M., 1995, Timing and velocity of petroleum migration in the Los Angeles Basin: Journal of Geology, v. 103, n. 1, p. 33–49, http://dx.doi.org/10.1086/629720

Helmig, R., 1997, Multiphase Flow and Transport Processes in the Subsurface: A Contribution to the Modeling of Hydrosystems: Berlin, Springer, 367 p.

Hesson, H. B., and Olilang, H. R., 1990, Seal Beach Oil Field: Alamitos and Marine Areas: Sacramento Division of Oil and Gas, California Department of Conservation, n. TR39, 14 p.

Higgins, C. T., and Chapman, R. H., 1984, Geothermal energy at Long Beach Shipyard and Naval Station and at Seal Beach Naval Weapons Station, Los Angeles and Orange Counties, California: California: California Department of Conservation, Division of Mines and Geology, DMG Open File Report 84-32, 72 p.

Hodgson, G. W., 1980, Origin of petroleum: In-transit conversion of organic compounds in water, *in* Roberts, W. H., III, and Cordell, R. J., editors, Problems of Petroleum Migration: AAPG Studies in Geology, v. 10, p. 169–178, http://dx.doi.org/10.1306/St10411C9

Hubbert, M. K., 1953, Entrapment of petroleum under hydrodynamics conditions: American Association of Petroleum Geologists Bulletin, v. 37, n. 8, p. 1954–2026.

Huber, R., and Helmig, R., 1999, Multiphase flow in heterogeneous porous media: A classical finite element method versus an implicit pressure explicit saturation-based mixed finite element finite volume approach: International Journal for Numerical Methods in Fluids, v. 29, n. 8, p. 899–920, http://dx.doi.org/10.1002/(SICI)1097-0363(19990430)29:8::AID-FLD7153.0.CO;2-W

_____ 2000, Node-centered finite volume discretizations for the numerical simulation of multiphase flow in heterogeneous porous media: Computational Geosciences, v. 4, n. 2, p. 141–164, http://dx.doi.org/10.1023/A:1011559916309

Hunt, J. M., 1979, Petroleum Geochemistry and Geology: San Francisco, California, W. H. Freeman, 617 p.

Ingebritsen, S. E., Neuzil, C. E., and Sanford, W. E., 2006, Groundwater in Geologic Processes: Cambridge, England, Cambridge University Press, 537 p.

Ingersoll, R. V., and Rumelhart, P. E., 1999, Three-stage evolution of the Los Angeles basin, southern California: Geology, v. 27, n. 7, p. 593–596, http://dx.doi.org/10.1130/0091-7613(1999)0272.3.CO;2

Jarvie, D. M., and Lundell, L. L., 2001, Kerogen type and thermal transformation of organic matter in the Miocene Monterey Formation, *in* Issacs, C. M., and Rullkötter, J., editors, The Monterey Formation: New York, Columbia University Press, p. 268–295.

Jeffrey, A. W. A., Alimi, H. M., and Jenden, P. D., 1991, Geochemistry of Los Angeles basin and gas system, *in* Biddle, K. T., editor, Active Margin Basins: AAPG Memoir, v. 52, p. 197–220.

Kaplan, I. R., Alimi, M. H., Hein, C., Jeffrey, A., Lafferty, M. R., Mankiewicz, M. P., Meredith, D. E., Edwards, E. B., and Dixon, W. S., 2000, The geochemistry of hydrocarbons and potential source rocks from the Los Angeles and Ventura basins, data synthesis and text, v. I, *in* Kaplan, I. R., editor, Collection of Papers Written in the Mid-to-Late 1980's and in 1997 by Staff Members of Global Geochemistry Corporation about the Oil, Gas, and Source Rock Investigations Carried Out in the San Joaquin, Santa Maria, Santa Barbara, Ventura, and Los Angeles Basins: California, Pacific Section - AAPG.

Karlsen, D. A., and Skeie, J. E., 2006, Petroleum migration, faults and overpressure, Part I: Calibrating basin modelling using petroleum in traps - A review: Journal of Petroleum Geology, v. 29, n. 3, p. 227–256, http://dx.doi.org/10.1111/j.1747-5457.2006.00227.x

Kestin, J., Khalifa, H. E., Sookiazian, H., and Wakeham, W. A., 1978, Experimental investigation of the effect of pressure on the viscosity of water in the temperature range 10-150 °C: Berichte Bunsengesellschaft für physikalische chemie, v. 82, n. 2, p. 180–188, http://dx.doi.org/10.1002/bbpc.197800008

Larter, S. R., Bowler, B. F., Li, M., Chen, M., Brincat, D., Bennett, B., Noke, K., Donohoe, P., Simmons, D., Kohnen, M., Allan, J., Telnaes, N., and Horstad., I., 1996, Molecular indicators of secondary oil migration distances: Nature, v. 383, n. 6601, p. 593–597, http://dx.doi.org/10.1038/383593a0

Leonard, R. C., 1984, Generation and Migration of Hydrocarbons on the Southern Norwegian Shelf, Geneva, Switzerland, AAPG Fossil Fuels of Europe Seminar: Bulletin of the American Association of Petroleum Geologists, v. 68, p. 796.

Levorsen, A. I., 1967, Geology of Petroleum: San Francisco, California, W. H. Freeman, 724 p.

Luyendyk, B. P., and Hornafius, J. S., 1987, Neogene crustal rotations, fault slip, and basin development in southern California, *in* Ingersoll, R. V., and Ernst, W. G., editors, Cenozoic basin development of coastal California: Englewood Cliffs, New Jersey, Prentice-Hall, p. 259–283.

Manzocchi, T., Childs, C., and Walsh, J. J., 2010, Faults and fault properties in hydrocarbon flow models: Geofluids, v. 10, n. 1–2, p. 94–113, http://dx.doi.org/10.1111/j.1468-8123.2010.00283.x

Mayer, L. A., 1991, Central Los Angeles Basin: subsidence and thermal implications for tectonic evolution, *in* Biddle, K. T., editor, Active Margin Basins: AAPG Memoir, v. 52, p. 185–196.

McCulloh, T. H., 1979, Implication for petroleum appraisal, *in* Cook, H. E., editor, Geologic Studies of the Point Conception Deep Stratigraphic Test Well OCS-CAL 78-164 No. 1 Outer Continental Shelf Southern California, United Sates: USGS Open File Report, n. 79–1218, p. 26-42.

McCulloh, T. H., Beyer, L. A., and Enrico, R. J., 2000, Paleogene strata of the eastern Los Angeles basin, California: Paleogeography and constraints on Neogene structural evolution: Geological Society of America Bulletin, v. 112, n. 8, p. 1155–1178, http://dx.doi.org/10.1130/0016-7606(2000)1122.0.CO;2

Mercer, J., Thomas, S. D., and Rose, B., 1982, Parameters and variables appearing in repository siting models: U. S. Nuclear Regulatory Commission, NUREG/CR-3086, 244 p.

Moshier, S. O., and Waples, D. W., 1985, Quantitative evaluation of Lower Cretaceous Mannville Group as source rock for Alberta's oil sands: American Association of Petroleum Geologists Bulletin, v. 69, n. 2, p. 161–172.

Munn, M. J., 1909, The anticlinal and hydraulic theories of oil and gas accumulation: Economic Geology, v. 4, n. 6, p. 509–529, http://dx.doi.org/10.2113/gsecongeo.4.6.509

Neuzil, C. E., 2003, Hydromechanical coupling in geologic processes: Hydrogeology Journal, v. 11, n. 1, p. 41–83, http://dx.doi.org/10.1007/s10040-002-0230-8

Nishikawa, T., Siade, A. J., Reichard, E. G., Ponti, D. J., Canales, A. G., and Johnson, T. A., 2009, Stratigraphic controls on seawater intrusion and implications for groundwater management, Dominguez Gap area of Los Angeles, California, USA: Hydrogeology Journal, v. 17, n. 7, p. 1699–1725, http://dx.doi.org/10.1007/s10040-009-0481-8

Norris, R. M., and Webb, R. W., 1990, Geology of California: New York, Wiley and Sons, Inc., 541p.

Perez, R. J., and Boles, J. R., 2007, Mineralization, fluid flow, and sealing properties associated with an active thrust fault: San Joaquin basin, California: American Association of Petroleum Geologists Bulletin, v. 88, n. 9, p. 1295–1314.

Person, M., and Garven, G., 1989, Hydrologic constraints on the thermal evolution of the Rhine Graben, *in* Beck, A. E., Garven, G., and Stegena, L., editors, Hydrogeological Regimes and Their Subsurface Thermal Effects: Geophysical Monograph Series, v. 47, p. 35–58, http://dx.doi.org/10.1029/GM047p0035

_____ 1992, Hydrologic constraints on petroleum generation within continental rift basins - theory and application to the Rhine Graben: American Association of Petroleum Geologists Bulletin, v. 76, n. 4, p. 468–488.

_____1994, A sensitivity study of the driving forces on fluid-flow during continental-drift basin evolution: Geological Society of America Bulletin, v. 106, n. 4, p. 461–475, http://dx.doi.org/10.1130/0016-7606(1994)1062.3.CO;2

Person, M., Banerjee, A., Rupp, J., Medina, C., Lichtner, P., Gable, C., Pawar, R., Celia, M., McIntosh, J., and Bense, V., 2010, Assessment of basin-scale hydrologic impacts of CO_2 sequestration, Illinois basin: International Journal of Greenhouse Gas Control, v. 4, n. 5, p. 840–854, http://dx.doi.org/10.1016/j.ijggc.2010.04.004

Pinder, G. F., and Gray, W. G., 1977, Finite Element Simulation in Surface and Subsurface Hydrology: New York, Academic Press, 295 p.

Pruess, K., 1991, TOUGH2 - A General Purpose Numerical Simulator for Multiphase Fluid and Heat Flow: Berkeley, California, Lawrence Berkeley Laboratory Report, v. LBL-29400, http://dx.doi.org/10.2172/5212064

Redin, T., 1991, Oil and gas production from submarine fans of the Los Angeles basin, *in* Biddle, K. T. editor, Active Margin Basins: AAPG Memoir, v. 52, p. 239–260.

Reichard, E. G., Land, M., Crawford, S. M., Johnson, T., Everett, R. R., Kulshan, T. V., Ponti, D. J., Halford, K. J., Johnson, T. A., Paybins, K. S., and Nishikawa, T., 2003, Geohydrology, geochemistry, and ground-water simulation-optimization of the central and west coast basins, Los Angeles County, California: U. S. Geological Survey, Water-Resources Investigation Report 03-4095.

Reichenberger, V., Jakobs, H., Bastian, P., and Helmig, R., 2006, A mixed-dimensional finite volume method for two-phase flow in fractured porous media: Advances in Water Resources, v. 29, n. 7, p. 1020–1036, http://dx.doi.org/10.1016/j.advwatres.2005.09.001

Rich, J. L., 1921, Moving underground water as a primary cause of the migration and accumulation of oil and gas: Economic Geology, v. 16, n. 6, p. 347–371, http://dx.doi.org/10.2113/gsecongeo.16.6.347

Ryan, W. B. F., Carbotte, S. M., Coplan, J. O., O'Hara, S., Melkonian, A., Arko, R., Weissel, R. A., Ferrini, V., Goodwillie, A., Nitsche, F., Bonczkowski, J., and Zemsky, R., 2009, Global multi-resolution topography synthesis: Geochemisty, Geophysics, Geosystems, v. 10, n. 3, Q03014, http://dx.doi.org/10.1029/2008GC002332

Sanford, R. F., 1995, Ground-water flow and migration of hydrocarbons to the Lower Permian White Rim Sandstone, Tar Sand Triangle, Southeastern Utah: USGS Bulletin, v. 2000-J, p. J1-J24.

Sass, J. H., Lachenbruch, A. H., Munroe, R. J., Greene, G. W., and Moses, T. H. J., 1971, Heat flow in the western United States: Journal of Geophysical Research, v. 76, n. 26, p. 6376–6413, http://dx.doi.org/10.1029/JB076i026p06376

Saywer, D. S., Albert, T. H., and Toksoz, M. N., 1987, Extension, subsidence and thermal evolution of the Los Angeles Basin - a two dimensional model: Tectonophysics, v. 133, n. 1–2, p. 15–32, http://dx.doi.org/10.1016/0040-1951(87)90277-0

Scheidegger, A. E., 1960, The Physics of Flow Through Porous Media: New York, Macmillan, 313 p.

Schoellhammer, J. E., Vedder, J. G., Yerkes, R. F., and Kinney, D. M., 1981, Geology of the northern Santa Ana Mountains, California: USGS Professional Paper, v. 420-D, p. D1–D109.

Shaw, J. H., and Suppe, J., 1996, Earthquake hazards of active blind-thrust faults under the central Los Angeles basin, California: Journal of Geophysical Research-Solid Earth, v. 101, n. B4, p. 8623–8642, http://dx.doi.org/10.1029/95JB03453

Sibson, R. H., 1977, Fault rocks and fault mechanisms: Journal of the Geological Society, London, v. 133, n. 3, p. 191–213. http://dx.doi.org/10.1144/gsjgs.133.3.0191

_____1994, Crustal stress, faulting and fluid flow, *in* Parnell, J., editor, Geofluids: Origin, Migration, and Evolution of Fluids in Sedimentary Basins: Geological Society, London, Special Publications, v. 78, p. 69–84, http://dx.doi.org/10.1144/GSL.SP.1994.078.01.07

Sorkhabi, R., and Tsuji, Y., 2005, The place of faults in petroleum traps, *in* Sorkahabi, R., and Tsuji, Y., editors, Faults, Fluid Flow, and Petroleum Traps: AAPG Memoir, v. 85, p. 1–31, http://dx.doi.org/10.1306/1033713M853128

Steckler, M. S., and Watts, A. B., 1978, Subsidence of the Atlantic-type continental margin off New York: Earth and Planetary Science Letters, v. 41, n. 1, p. 1–13, http://dx.doi.org/10.1016/0012-821X(78)90036-5

Swarbrick, R. E., Osborne, M. J., and Yardley, G. S., 2002, Comparison of overpressure magnitude resulting from the main generating mechanisms, *in* Huffman, A., and Bowers, G., editors, Pressure Regimes in Sedimentary Basins and their prediction: AAPG Memoir, v. 76, p. 1–12.

Tissot, B. P., and Welte, D. H., 1984, Petroleum Formation and Occurrence: New York, Springer-Verlag, 699 p.

Tissot, B. P., Pelet, R., and Ungerer, P., 1986, Thermal history of sedimentary basins and kinetics of oil and gas generation: American Association of Petroleum Geologists Bulletin, v. 70, n. 5, p. 656–656.

_____ 1987, Thermal history of sedimentary basins, maturation indexes, and kinetics of oil and gas generation: American Association of Petroleum Geologists Bulletin, v. 71, n. 12, p. 1445–1466.

Tóth, J., 1980, Cross-formational gravity-flow of groundwater: a mechanism of the transport and accumulation of petroleum (the generalized hydraulic theory of petroleum migration), *in* Roberts, W. H., III, and Cordell, R. J., editors, Problems of Petroleum Migration: AAPG Studies in Geology, p. 121–167.

_____ 1987, Petroleum hydrogeology: a new basic in exploration: World Oil, v. 205, n. 3, p. 48–50.

_____ 1988, Ground water and hydrocarbon migration, *in* Rosenshein, J. S., and Seaber, P. R., editors, Hydrogeology: The Geological Society of America, Geology of North America, v. O-2, p. 485–502.

_____ 2009, Gravitational Systems of Groundwater Flow: Theory, Evaluation, Utilization: Cambridge, England, Cambridge University Press, 297 p.

Ungerer, P., Burrus, J., Doligez, P., Chenet, P. Y., and Bessis, F., 1990, Basin evaluation by integrated two-dimensional modeling of heat transfer, fluid flow, hydrocarbon generation and migration: American Association of Petroleum Geologists Bulletin, v. 74, n. 3, p. 309–335.

van Genuchten, M. T., 1980, A closed-form equation for predicting the hydraulic conductivity of unsaturated soils: Soil Science Society of America Journal, v. 44, n. 5, p. 892–898, http://dx.doi.org/10.2136/sssaj1980.03615995004400050002x

van Hinte, J. E., 1978, Geohistory analysis - application of micropaleontology in exploration geology: American Association of Petroleum Geologists Bulletin, v. 62, n. 2, p. 201–222.

Welte, D. J., and Yükler, A., 1980, Evolution of sedimentary basins from the standpoint of petroleum origin and accumulation -an approach for a quantitative basin study: Organic Geochemistry, v. 2, n. 1, p. 1–8, http://dx.doi.org/10.1016/0146-6380(80)90016-9

Wendebourg, J., ms, 1994, Simulating hydrocarbon migration and stratigraphic traps: Stanford, California, Stanford University, Ph. D. thesis, 258 p.

Williams, C. F., Beyer, L. A., Grubb, F. V., and Galanis, S., 2001, Heat flow and the seismotectonics of the Los Angeles and Ventura basins of Southern California: San Francisco, California, December 10-14, AGU 2001 Fall Meeting, Abstract #S11A-0534.

Wilson, A. M., Garven, G., and Boles, J. R., 1999, Paleohydrogeology of the San Joaquin basin, California: Geological Society of America Bulletin, v. 111, n. 3, p. 432–449, http://dx.doi.org/10.1130/0016-7606(1999)1112.3.CO;2

Wright, T. L., 1991, Structural geology and tectonic evolution of the Los Angeles Basin, California, *in* Biddle, K. T., editor, Active Margin Basins: AAPG Memoir, v. 52, p. 35–134.

Yerkes, R. F., 1972, Geology and oil resources of the western Puente Hills area, southern California: USGS Professional Paper, v. 420-C, p. 63.

Yerkes, R. F., McCulloh, T. H., Schoellhammer, J. E., and Vedder, J. G., 1965, Geology of the Los Angeles basin, California - an introduction: USGS Professional Paper, v. 420-A, p. A1–A57.

Zienkiewicz, O. C., 1977, The Finite Element Method: London, New York, McGraw-Hill, 787 p.